
Electronic Thesis and Dissertation Repository

9-6-2017 2:45 PM

Investigating Growth of Metal-Organic Frameworks via Atomic Force Microscopy

Zitong Wang

The University of Western Ontario

Supervisor

Yining Huang

The University of Western Ontario

Graduate Program in Chemistry

A thesis submitted in partial fulfillment of the requirements for the degree in Master of Science

© Zitong Wang 2017

Follow this and additional works at: <https://ir.lib.uwo.ca/etd>

 Part of the [Chemistry Commons](#)

Recommended Citation

Wang, Zitong, "Investigating Growth of Metal-Organic Frameworks via Atomic Force Microscopy" (2017).
Electronic Thesis and Dissertation Repository. 4878.

<https://ir.lib.uwo.ca/etd/4878>

This Dissertation/Thesis is brought to you for free and open access by Scholarship@Western. It has been accepted for inclusion in Electronic Thesis and Dissertation Repository by an authorized administrator of Scholarship@Western. For more information, please contact wlsadmin@uwo.ca.

Abstract

Metal-organic frameworks (MOFs) are crystalline microporous materials that have drawn much attention in recent years for their promising applications in many fields of chemistry. To design MOFs with desired properties, a better understanding of how these frameworks self-assemble during crystallization is required. A useful technique for investigating the crystallization process of MOFs is atomic force microscopy (AFM). We have conducted AFM studies on four different MOFs: the gallium analog of the MIL-53 MOF, which exhibits the "breathing effect," and three Lead, Calcium and Cadmium-based MOFs that uses 4,4-sulfonyldibenzoate (SDB) as the organic ligand. Hydrothermal methods were used to prepare those materials, and their surface features and growth mechanisms were discussed. By exploring possible termination structures on the surfaces, we can also probe the fundamental growth units as they self-assemble to form these 3-D microporous frameworks.

Keywords

Metal-Organic frameworks, growth mechanism, surface structure, crystallization, Ga-MIL-53, PbSDB, CaSDB, CdSDB, atomic force microscopy

Co-Authorship Statement

Some of the crystals were provided by Jason Zhang and Shoushun Chen in Dr. Yining Huang's group. Jason Zhang is also credited for performing SEM experiments used in this thesis.

Acknowledgments

First of all, I would like to thank my supervisor, Dr. Yining Huang. I have benefited a lot from his guidance and expertise during the last two years. Words fail me to express my gratitude to him, and without his constant support and patience, I would not have finished this thesis.

I would like to sincerely thank Dr. Heng-Yong Nie at Surface Science Western who trained me to use AFM. His continuous support forms the foundation of this study.

Thanks also goes to Dr. Paul Boyle and Dr. Roberta Flemming. I learned so much about crystallography and X-ray diffraction techniques from their great lectures.

My gratitude also goes to my past and current colleagues in the Huang group. They are Bryan E.G. Lucier, Jason Zhang, Shoushun Chen, Shan Jiang, Yuanjun Lu, Bowei Wu, Bligh Desveaux, Hendrick Chan, Tetyana Levchenko, Yue Hu and Donghan Chen. Their friendship and support have made my experience at Western so much more enjoyable.

Finally, a special thanks to my parents, Qi Wang and Ren Wang, for their unconditional love and non-stop support.

Table of Contents

Abstract	i
Co-Authorship Statement.....	ii
Acknowledgments.....	iii
Table of Contents	iv
List of Tables	vii
List of Figures	viii
List of Abbreviation.....	xii
Chapter 1	1
1 Introduction.....	1
1.1 Metal-Organic Frameworks	1
1.2 Crystal Growth Mechanisms.....	2
1.3 Miller Index Notation	5
1.4 Crystal Habit and Its Prediction.....	6
1.5 Atomic Force Microscopy	8
1.6 AFM studies on MOFs.....	11
1.7 Outline and Motivation of the Thesis	13
1.8 References.....	14
Chapter 2.....	20
2 Experimental	20
2.1 MOF Sample Preparation	20
2.2 Characterization Methods	21
2.2.1 Atomic Force Microscopy	21
2.2.2 Powder X-ray Diffraction	23
2.2.3 Scanning Electron Microscopy	24

2.3	References.....	24
Chapter 3	26
3	An Investigation of Crystal Growth of Metal-Organic Framework Ga-MIL-53.....	26
3.1	Introduction.....	26
3.2	Experimental.....	27
3.2.1	Sample Preparation	27
3.2.2	Characterization	28
3.3	Results and Discussion	29
3.3.1	Surface Observation on {101} face	29
3.3.2	Crystal Growth of Ga-MIL-53 at Different Length of Time	37
3.3.3	Crystal Growth of Ga-MIL-53 with different Ga:BDCA ratio.....	42
3.3.4	Investigations on Surface Changes of Ga-MIL-53 Induced by “Breathing Effect”	47
3.4	Conclusion	52
3.5	References.....	53
Chapter 4	56
4	Investigating Crystal Growth of M-SDB Metal-Organic Frameworks	56
4.1	Introduction.....	56
4.2	Experimental.....	59
4.2.1	Sample Preparation	59
4.2.2	Characterization	60
4.3	Results and Discussion	61
4.3.1	PbSDB.....	61
4.3.2	CaSDB	67
4.3.3	CdSDB	74
4.4	Conclusion	77

4.5 References.....	78
Chapter 5.....	81
5 Summary and Future Works	81
5.1 Summary.....	81
5.2 Future Works	82
5.3 References.....	83
Appendices.....	85
Curriculum Vitae	89

List of Tables

Table 3-1 Summary of synthesis conditions used in successful attempts.	28
Table 4-1 Summary of synthesis conditions of CaSDB	59

List of Figures

Figure 1-1 Kossel model showing different attachment sites. ²⁹	3
Figure 1-2 Simplified scheme showing (a) “adhesive type growth” mechanism, (b) “birth and spread” mechanism and (c) “spiral growth” mechanism. ²⁸	4
Figure 1-3 (a) Three basic forms of class mmm.(b) Three different habits of barite found in different regions of England, showing different present forms: a{100}, b{010}, c{001}, m{110}, d{102} and o{011}. ³²	7
Figure 1-4 Diagram of conventional AFM scanning.....	8
Figure 1-5 Interaction force versus distance for two atoms.....	10
Figure 1-6 Cross-sectional analysis of a typical step train on the {111} face of HKUST-1 (a) and the structure of HKUST-1 viewed down a [110] direction highlighting possible d_{111} and d_{222} crystal spacings (b). ³⁶	11
Figure 1-7 In situ AFM measurements on {110} face of ZIF-8 crystal reveal growth steps formed from (a) “birth and spread” mechanism and (b) spiral mechanism. The consistent step height of 1.2 nm related to the d_{110} spacing is found from the cross-sectional analysis in (c). (d) illustrates the structure of ZIF-8 viewed along [100] direction. ³⁷	12
Figure 2-1 Scheme showing the set-up of a hydrothermal synthesis.....	20
Figure 2-2 Schemes showing the sample preparation process.....	22
Figure 2-3 Comparison between an error image (Left) and a topography image (Right). The two images feature the same region of a MOF crystal. Those images are processed using Gwyddion software.	23
Figure 3-1 (a) shows the octahedral $\text{MO}_4(\text{OH})_2$ secondary building unit; (b) shows the chain formed along b axis. A rhombus channel along b axis is demonstrated in (c). (d) shows the structure of the benzenedicarboxylate linker.	27

Figure 3-2 (Left) An overview of Ga-MIL-53 single crystals from SEM. (Middle) A zoomed in SEM micrograph featuring one single Ga-MIL-53 crystal. (Right) Scheme showing habit prediction.	30
Figure 3-3 (a-b) AFM error images of Ga-MIL-53 after 3 days of synthesis; (c) optical image showing the single crystal that was being scanned.	31
Figure 3-4 AFM error images of Ga-MIL-53 after 3 days of synthesis; (a) a growth hillock on a $\{101\}$ face; (b) zoomed in image showing the area enclosed in the box on (a). (c) describes the orientation of the $\{101\}$ face studied and (d) shows the height profile acquired along the line in (a).	32
Figure 3-5 The MIL-53(Ga) structure viewing through the rhombus channel. Hydrogen atoms are omitted for clarity.	33
Figure 3-6 (a-c) Error images showing a spiral growth hillock at different scales. (d) A 3D representation of the spiral growth hillock. (e) Height profile along the blue line in c.	35
Figure 3-7 AFM deflection images of $\{101\}$ face after re-grown treatment. (d) is the zoom in image of the blue box in (c). (e) and (f) are height profiles measured along the blue line and black line in (c), respectively.	36
Figure 3-8 Powder X-ray diffraction patterns for Ga-MIL-53 crystallites with different synthesis times.	38
Figure 3-9 (a-b) Error images captured on samples with 1 day synthesis time. (c) Height profile captured along the blue line in (a).	39
Figure 3-10 (a-c) Schemes showing relationships between growth rates in different terrace morphologies. (d) a layered hillock indicating the transition from hexagonal to rectangular.	40
Figure 3-11 (Left) 2-D representation of a $\{101\}$ layer using a Kossel model, where growth units are described as squares. (Right) Schematic representation of a single $\{101\}$ layer which composes of Ga-O-Ga inorganic chain along $[010]$ bridged by BDC.	41

Figure 3-12 AFM error images from 1:1, 1:1.5, 1:2, and 1:4 syntheses. All syntheses were conducted for a duration of 3 days.....	44
Figure 3-13 Comparison of layer morphologies from 1:1 and 1:2 synthesis experiments with same BDCA starting concentration. (a) is a topography image and (b-d) are error images...	46
Figure 3-14 The MIL-53(Ga) structure for three phases. Hydrogen atoms are omitted for clarity.	48
Figure 3-15 AFM error images and SEM micrographs on Ga-MIL-53_dmf (a-b) and Ga-MIL-53_lt (c-d). (e) is a schematic representation of a single {101} layer.....	49
Figure 3-16 (a) AFM error image captured on Ga-MIL-53_dmf. (b) AFM error image captured on Ga-MIL-53_lt. Height profiles along the blue lines are shown on the right of corresponding images.	51
Figure 4-1 Structure of the V-shaped SDB ligand.....	56
Figure 4-2 (Left) structure of PbSDB viewed along a axis; (Right) Local structure and Lead coordination environment of PbSDB.....	57
Figure 4-3 (Left) structure of CaSDB viewed along b axis; (Right) Local structure and Calcium coordination environment of CaSDB.....	57
Figure 4-4 (Left) structure of CdSDB viewed along c axis; (Right) Local structure and Cadmium coordination environment of CdSDB.....	58
Figure 4-5 Scanning electron micrographs of PbSDB single crystals revealing {001} and {011} facets.	61
Figure 4-6 (a) is an overview of a {011} face and (b) and (c) are the zoom in images showing rectangular growth hillocks and elongated nuclei. (d) shows the height profile measured along the blue line in (b). (e) describes the orientation of the {011} face scanned.....	62
Figure 4-7 PbSDB framework structure viewing through [100] direction.	64

Figure 4-8 (a) shows the optical microscopic image with a $\{002\}$ face on top. (b), (c), (d), (e) and (f) are AFM deflection image captured from different regions of the $\{002\}$ face in (a). The zoomed in image of the blue box in (d) is shown in (f). (g) is a scheme showing layer pattern on the surface. (h) shows cross-section analyses taken along the black line in (f).....	65
Figure 4-9 PbSDB framework structure viewing through $[100]$ direction. The black box represents the unit cell.	67
Figure 4-10 Two different crystals of CaSDB from synthesis A under optical microscope. .	68
Figure 4-11 AFM deflection images captured on the surface of CaSDB from synthesis A. (a) was taken from the single crystal shown in Figure 4-10a; (b)-(d) were taken from the single crystal in Figure 4-10b. (e) and (f) are cross-sectional profiles along the line in (c) and (d), respectively.	69
Figure 4-12 (a) and (b) are AFM deflection images and (c) is a topology image captured on the surface of CaSDB, showing triangular-like terraces. (d) and (e) are cross-sectional profiles along the black lines in (a) and (b), respectively.	71
Figure 4-13 CaSDB framework structure viewing through $[010]$ direction. The black box represents the unit cell.	72
Figure 4-14 AFM deflection images of $\{110\}$ surface of CdSDB. (c) is the optical image of the single crystal being scanned.	74
Figure 4-15 (a), (c-e) are the AFM deflection images captured on the surface of CdSDB and (b) is the single crystal's optical image. (c), (d), and (e) were captured from different regions on (a). (f) and (g) are cross-sectional profiles along the line in (c) and (e), respectively.	75
Figure 4-16 CdSDB framework structure viewing through $[001]$ direction. The black box represents the unit cell.	76

List of Abbreviation

as	As-made
AFM	Atomic force microscopy
BDC	1, 4-benzenedicarboxylate
BDCA	1, 4-benzenedicarboxylic acid
BFDH	Bravais-Friedel-Donnay-Harker
DMF	Dimethylformamide
lt	Low temperature
MOF	Metal-Organic framework
SDB	4, 4-sulfonyldibenzoate
SDBA	4, 4-sulfonyldibenzoic acid
SPM	Scanning probe microscopy
XRD	X-ray diffraction
ZIF	Zeolitic imidazolate framework
1D	One dimensional

Chapter 1

1 Introduction

1.1 Metal-Organic Frameworks

Metal-organic frameworks (MOFs) are a type of hybrid crystalline nanoporous materials. MOFs have fascinating properties such as thermal stability, storage capability, and most importantly their ultrahigh porosity, with surface areas extending beyond 6000 m²/g.¹⁻² In comparison with the widely used sorbents namely zeolites, the surface area of zeolites rarely exceeds 1000 m²/g.³ Due to their promising potentials for gas storage and separation, drug delivery and catalysis, MOFs have attracted significant interests.⁴⁻¹⁰ A large number of new structures are reported every year.^{2, 11}

Generally, MOF materials are composed of two parts; secondary building units (SBUs) containing metal centers or clusters which are connected by organic linkers by strong bonds, leading to the construction of 3D porous networks. The properties of MOF are tunable by the structure and composition of the framework, and the numerous choices of metal ions and organic linkers have led to many possibilities of MOF's topologies and connectivity.¹² The variability of MOFs has allowed the synthesis with specific designed functions and applications.¹³⁻¹⁴ For example, Al¹⁵, Cr¹⁶, Ga¹⁷, Fe¹⁸, Sc¹⁹ and In²⁰ are all capable of generating a flexible network with MIL-53 topology when combined with 1,4-benzendicarboxylate (BDC) as organic ligand, and the properties of the frameworks with varied metal centers have been extensively studied.²¹⁻²² On the other hand, replacing or modifying ligands is another common yet useful approach to tune the properties of isorecticular MOFs.^{12, 23-25} In order to produce MOFs with larger pore size, elongation of

the ligands is usually employed.²⁶ Another example of improving the performance of MOFs without altering metal-containing units is functionalization of the ligand. For instance, the water stability of some MOFs can be significantly increased when the ligand is functionalized with hydrophobic groups.²⁷

Synthesis of MOFs has been achieved *via* a variety of methods such as solvothermal, electrochemical, mechanochemical, sonochemical and microwave-assisted methods.¹² Among them, solvothermal method is a conventional and one of the most commonly used methods to synthesize MOFs. A typical solvothermal synthesis usually takes place in a closed system (e.g. sealed steel autoclave), where the reagents are mixed in an aqueous solvent and heated above the boiling point of the solvent. In cases when the temperature is below the boiling point of the solvent, the synthesis is referred to as nonsolvothermal. The process of crystal growth is dependent on various reaction conditions including the concentration of the reactants, temperature, the length of reaction and choice of the solvent. Varying one or several of those reaction conditions may give rise to different particle size, crystal habit, reaction yield and crystallinity of the product, which in turn may have an effect on the properties of the material.¹² Thus with a better understanding in crystallization of MOFs, synthesis could be tailored to accommodate the desired properties of those materials.

1.2 Crystal Growth Mechanisms

The mechanisms of crystal growth on a surface are very complicated as more than one type of attachment sites may be present. One commonly used model to describe the crystal surface is the Kossel model.²⁸ The model treats the growth unit of the material as a simple cube which has six unsaturated bonding sites, each aligning perpendicular to one of the

cube's six faces. Sites could be classified into different types based on the number of bonds formed between themselves and the growth unit upon attachment, which is shown in Figure 1-1. For growth units that are attaching to the terrace, only one of their six faces will be in contact with the crystal, thus forming one bond. In comparison, there will be two and three bonds formed in edge sites and kink sites, respectively. With the same idea, four potential bonding sites will be utilized for growth units attaching into the surface vacancy. Since the formation of the bond decreases the free energy of the system, the attachment to the vacancy sites will be the most favorable.

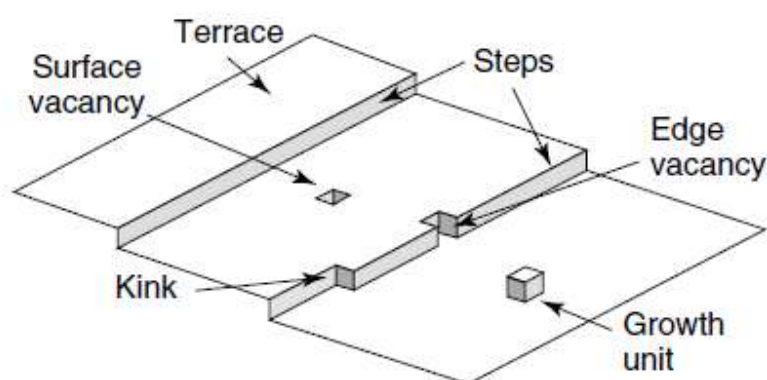


Figure 1-1 Kossel model showing different attachment sites.²⁹

A crystal model that is made of such cubic growth units is called the Kossel crystal. Interfaces on a Kossel crystal can be differentiated depending on whether they are atomically smooth or rough. The surface is defined as flat (F face), stepped (S face) or kinked (K face) based on the bonding sites that it consists of. Since the attachment energy is proportional to growth rate, the kinked faces will grow faster than the stepped faces, and the flat faces will be the slowest growing faces among the three.

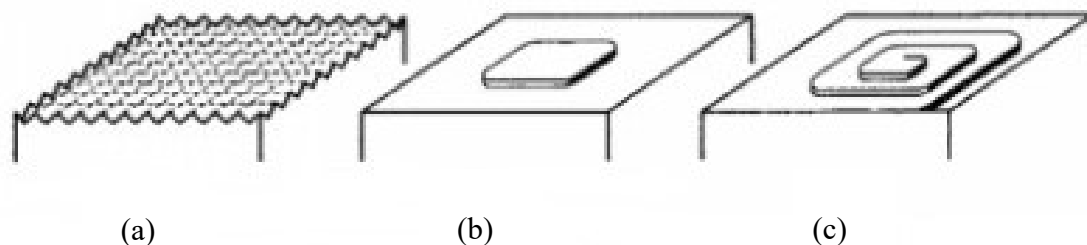


Figure 1-2 Simplified scheme showing (a) “adhesive type growth” mechanism, (b) “birth and spread” mechanism and (c) “spiral growth” mechanism.²⁸

For crystal growth occurring on a smooth interface, the most common mechanism is the “birth and spread” mechanism, also known as the “layer by layer” mechanism. Under this mechanism, the growth is initiated by 2-dimensional nucleation on the surface. Once the nucleation is finished, the nucleus provides stepped sites or kinked sites for the incoming growth units to attach. In this way, the face will grow by the 2-dimensional spreading of the step. After the layer is completed new nucleus will be required to function as step sources. However, in real cases, the observations on different MOF crystals show that nucleation and 2D spreading of the step could occur simultaneously. As a result, terraces originated from different nucleus will coalesce when they meet each other, contributing to a variety of surface morphologies.

Since nucleation requires more energy than the attachment of growth units onto stepped sites or kinked sites, nucleation is the prerequisite for growth following the “birth and spread” mechanism to occur. If supersaturation drops to a level that the driving force fails to overcome the energy barrier required to nucleate, the growth is expected to terminate.

However, growth has been observed on crystals with a degree of supersaturation lower than that needed for nucleation to take place.²⁸ It is found that crystal growth under those conditions follows a distinct mechanism called “spiral mechanism,” where a previously formed screw dislocation acts as the step source. Under this mechanism, the surface grows by the advancement of the steps around the dislocation core like a “spiral staircase”. New kink sites are created perpetually as the spiral grows, and nucleation is no longer needed.

The “birth and spread” and “spiral growth” are both mechanisms for growth on a smooth surface. At very high supersaturation, which usually happens at the early stage of crystallization, the surface becomes rough, and the growth is called to be “adhesive type growth”.²⁸⁻²⁹ The rough surfaces consist of kink sites, and growth units arriving at such a surface will be readily incorporated into the crystal. As a result, the surface grows homogeneously rather than two-dimensionally.

1.3 Miller Index Notation

Miller indices are a very useful notation system in crystallography, and it will be used to describe crystallographic planes and directions throughout the thesis. Generally three brackets are used in this notation:³⁰

Square brackets are used to describe a crystallographic direction. For example, $[100]$, $[010]$, and $[001]$ denote three directions along the crystal axes x , y , and z , respectively.

A plane that intercepts a/h , b/k and c/l with the axes are denoted with round brackets as (hkl) , where a , b and c are unit cell vectors. When a number of planes are crystallographically equivalent and indistinguishable, they can be classified into a group using curly brackets. A simple example can be made using the cubic system, where the six faces denoted as

(100) , (010) , (001) , $(\bar{1}00)$, $(0\bar{1}0)$, $(00\bar{1})$ can all be expressed with the single notation $\{100\}$.

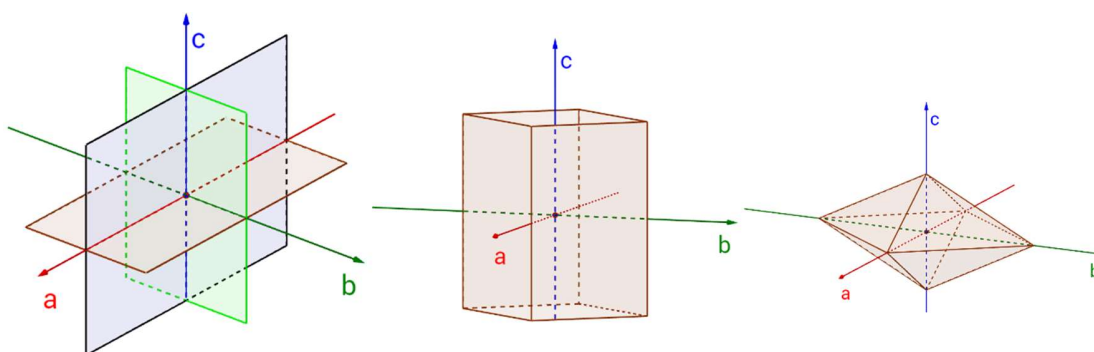
1.4 Crystal Habit and Its Prediction

The shape that a crystal could develop is called the crystal habit.³¹ The habit can be described by sets of crystal faces that are related by symmetry known as crystal forms. The characteristics—forms that a polyhedral crystal has is usually determined by the internal symmetry such as the point groups and the size and form of the unit cell, but are also highly dependent on the growth environment. In other words, crystals can develop different habits under different conditions, but their forms are all limited by the same internal symmetry. For example, under class mmm of the orthorhombic crystal system, there are three basic forms: $\{100\}$ pinacoids, $\{hk0\}$ prisms and $\{hkl\}$ bipyramids (Figure 1-3a).³¹ Barium sulfate, also known as a common mineral barite, belongs to this symmetry class. Figure 1-3b shows that with the same composition, the habit does not stay constant when crystallizing under different environments.³²

(a) $\{100\}$ pinacoids

$\{hk0\}$ prisms

$\{hkl\}$ prisms



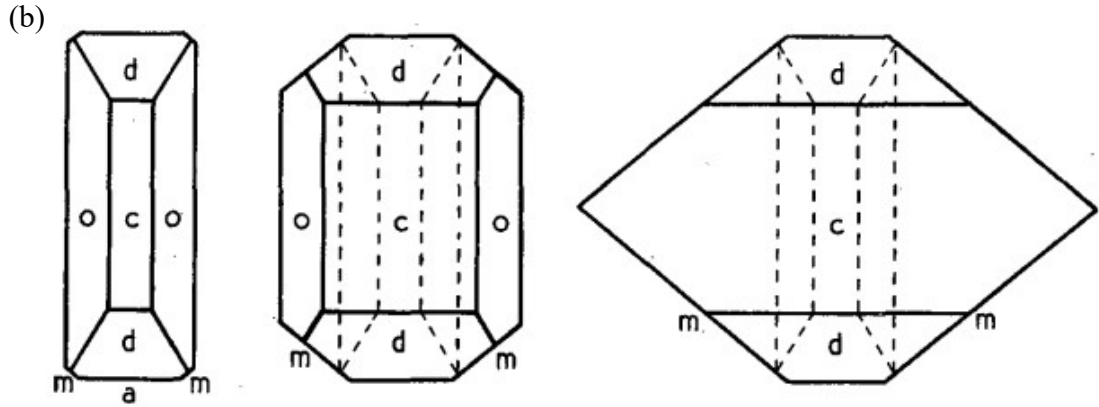


Figure 1-3 (a) Three basic forms of class mmm.(b) Three different habits of barite found in different regions of England, showing different present forms: $a\{100\}$, $b\{010\}$, $c\{001\}$, $m\{110\}$, $d\{102\}$ and $o\{011\}$.³²

In our AFM studies, before we can relate the observed nano-scaled surface features to the plausible height differences in the crystal structure, it is very necessary to make reasonable predictions on the crystal habit.

One commonly used method to predict crystal habit is by employing the BFDH law.³³ The law is named after Bravais, Friedel, Donney and Parker, which assumes that the slowest growing faces are the ones with the longest inter-planar distance. The relationship can be described as

$$R_{hkl} \propto 1/d_{hkl}$$

where R_{hkl} is the growth rate of crystallographic plane hkl in the direction that normal to itself and d_{hkl} is its inter-planar spacing. Since faces that grow faster will disappear first, the most predominant faces are those with the longest inter-planar spacing. Besides that, the method also takes the extinction conditions of the space group into account and has been found to give reasonable predictions confirmed by experimental observations.³⁴

1.5 Atomic Force Microscopy

As a member of Scanning Probe Microscope (SPM), Atomic Force Microscopy (AFM) is a powerful tool to visualize and measure microscopic surface structure. Different from other types of microscopes, an SPM can image the topology of the substance of interest with a high resolution. Typically, the best resolution that can be achieved for an SPM is 0.1 nm in the z direction.³⁵

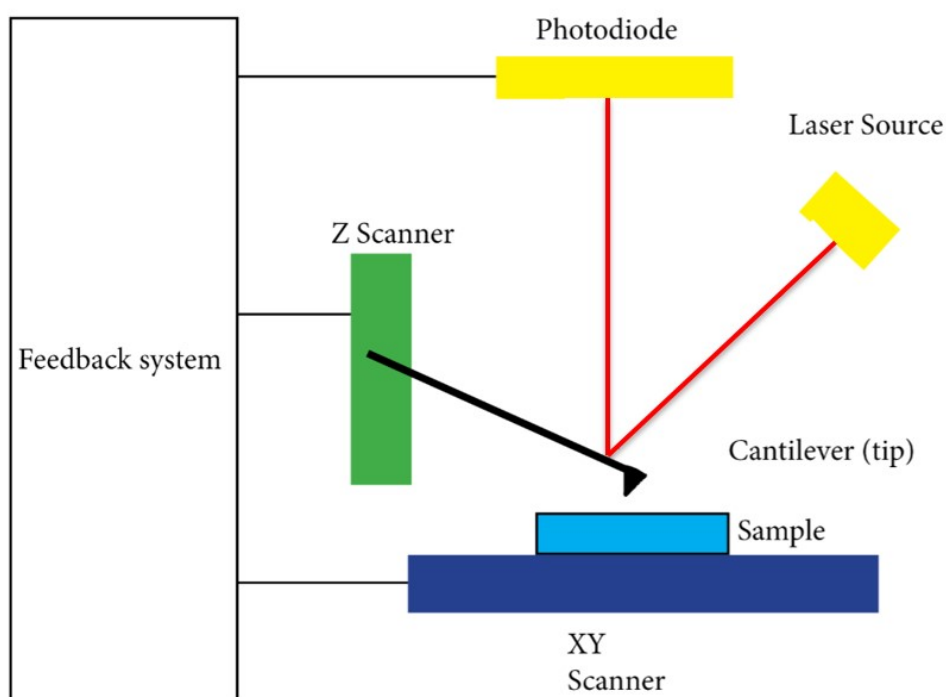


Figure 1-4 Diagram of conventional AFM scanning.

The instrument images by using the physical interaction between a sharp tip and the surface. The tip is attached to a flexible force-sensing cantilever which scans over the surface in a raster pattern. Unlike the other member of SPM, Scanning Tunneling

Microscope (STM), which relies on the tunneling current between the metallic tip and the surface, AFM does not require the surface to be conductive. In AFM, the interaction between the tip and the surface can be rationalized using the Lennard-Jones potential, which is a simple model that describes the interaction potential between two neutral atoms or molecules. The Lennard-Jones potential is defined as:

$$w(r) = -A/r^6 + B/r^{12}$$

where A and B are constants known to be 10^{-77}Jm^6 and 10^{-134}Jm^{12} and r is the distance between the two atoms. In turn, we are also able to define the interaction force:

$$F = -dw(r)/dr = -6A/r^7 + 12B/r^{13}$$

It can be seen that the interaction force is attractive when the separation distance is around 0.4 nm (Figure 1-5). As the two atoms draw closer and the closer, the force increases dramatically thereafter. The relationship between interaction force and distance is the principle that enables AFM to retrieve the height profile of the surface. However, in reality, the interaction between the tip and the surface could be much larger since the tip has numerous atoms at the pointy end.

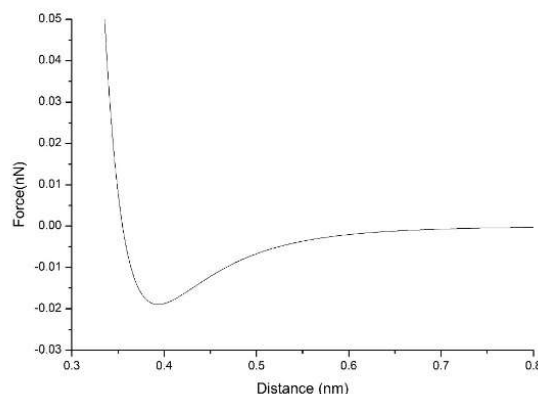


Figure 1-5 Interaction force versus distance for two atoms.

The accurate movement and positioning of the cantilever are achieved by the piezoelectric scanner it is attached to. During the scan, the physical force between the tip and the surface causes the cantilever to deflect. And by monitoring the deflection of the cantilever using a laser beam and a photodiode detector, the distance between the tip and the surface could be known, from which the topology of the sample surface can then be retrieved.

Currently, there are two primary working modes for AFM: contact mode and dynamic force mode. In contact mode, the tip is physically in contact with the surface. The height of the tip is adjusted to keep the interaction force between the tip and the surface constant. On the other hand, in the tapping mode or the dynamic force mode, the cantilever is oscillating around its resonance frequency, and the height is adjusted to maintain a constant amplitude and distance. Right operation mode should be selected prior to experiment to make the best use of its strengths: the contact mode is advantaged for being able to record the lateral force and surface stiffness, while the tapping mode does the least damage to the surface.

1.6 AFM studies on MOFs

AFM's nano-scaled resolution has allowed the observation of the smallest building unit during the growth process, and the surface growth patterns also provide information about growth mechanisms. Applications of AFM on discovering crystallization processes of microporous materials were initially conducted on zeolites, both natural and synthetic ones. The results have been fruitful; nano-scale features such as terrace shape and height observed on different facets yield useful information about pore arrangement and growth mechanism.

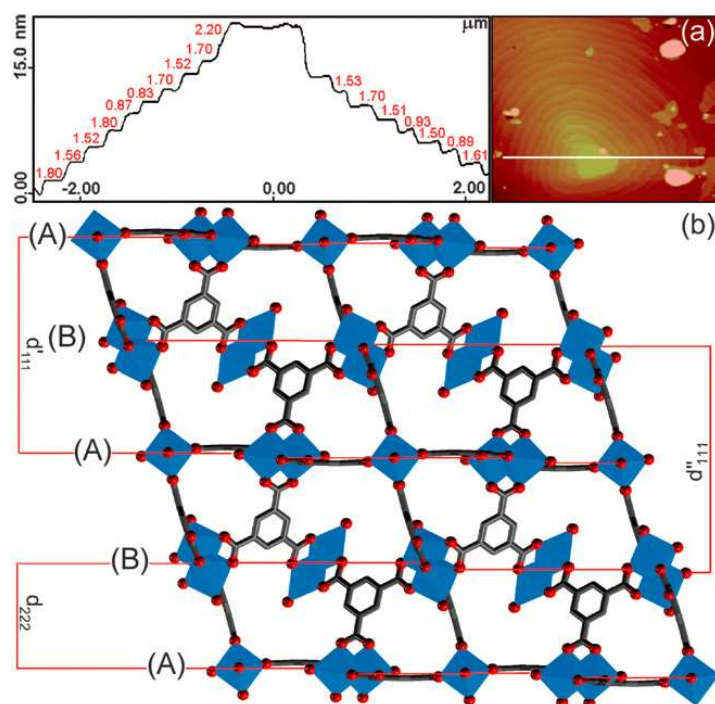


Figure 1-6 Cross-sectional analysis of a typical step train on the {111} face of HKUST-1 (a) and the structure of HKUST-1 viewed down a [110] direction highlighting possible d_{111} and d_{222} crystal spacings (b).³⁶

The first AFM investigation on MOF was conducted by Shöâeè *et al* on the well-known MOF HKUST-1.³⁶ Surfaces of {111} facets were imaged using *ex-situ* AFM, and three-

fold growth hillocks were observed which could be related to the symmetry elements of the lattice. A closer inspection of the growth hillocks revealed that they were spirals emanated from dislocations. Cross-sectional analysis on the spirals was then conducted, showing a consistent step height of 1.5 nm corresponding to the d_{111} spacing. Even though extended layers could be clearly seen, the *ex-situ* measurement does not give decisive evidence about surface termination, as there are two possibilities for the steps to possess the height of d_{111} spacing without bond breaking within the trimesate moieties. The two possible termination layers are shown in Figure 1-6 labeled as A and B. Surface termination at the layer of octahedra A would leave one unused bonding site per Cu, where surface termination at the layer of octahedra B would leave two bonding sites per Cu not integrated into the framework. Therefore the extended step observed was more likely to be terminated by layer B since it is more stable than the layer of type A.

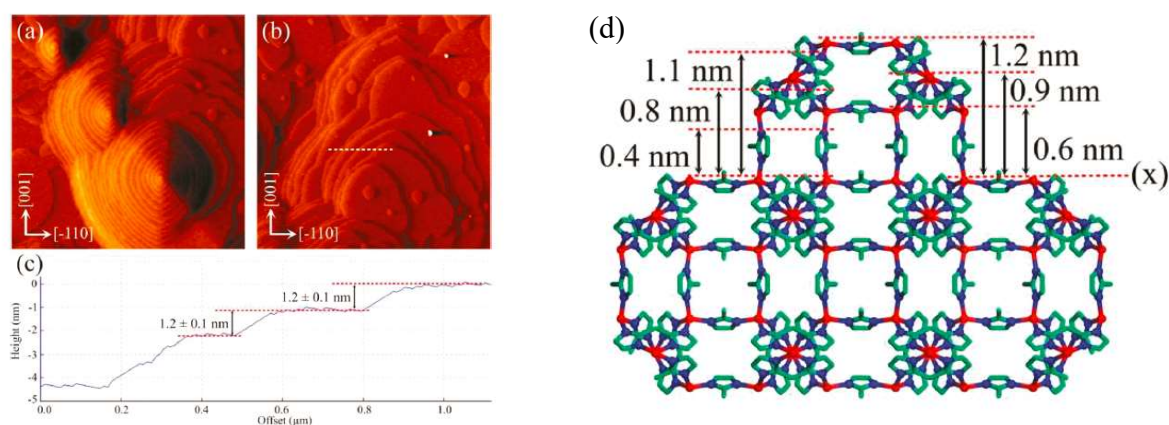


Figure 1-7 In situ AFM measurements on {110} face of ZIF-8 crystal reveal growth steps formed from (a) “birth and spread” mechanism and (b) spiral mechanism. The consistent step height of 1.2 nm related to the d_{110} spacing is found from the cross-sectional analysis in (c). (d) illustrates the structure of ZIF-8 viewed along [100] direction.³⁷

Ex-situ AFM experiments could yield detailed information which reveals nano-scaled features on the growing surface and provide clear evidence about growth mechanism. However, they are conducted on isolated crystals, where surface features result from both growth and dissolution process. In addition, since *ex-situ* observations are not the real time monitoring of crystal growth process, sometimes the exact composition of the observed stable steps cannot be determined. A good example of *in-situ* AFM experiments was conducted on ZIF-8, which successfully reveals the details about the formation of stable surface steps.³⁷ The framework of ZIF-8 adopts a sodalite topology and is constructed from corner sharing $\text{Zn}(\text{MeIm})_4$ units (Figure 1-7d). AFM scan on the $\{110\}$ facets found both growth spirals and growth hillocks formed by “birth and spread” mechanism indicating that crystal growth follows those two mechanisms at the same time. Cross-sectional analysis shows that the steps have a uniform height of 1.2 nm, which agrees with the d_{110} crystal spacing. The fundamental units involved in the assembly process of those 1.2 nm steps were revealed by *in situ* monitoring of crystal growth. It is found that newly born nuclei were firstly observed to have the height of 0.4 nm, which is due to the addition of MeIm^- ions on layer x in Figure 1-7d. As the growth continues, the nuclei develop into heights of 0.6, 0.8, 0.9, 1.1 and 1.2 nm which are from the further addition of MeIm^- and Zn^{2+} ions on the incomplete cages.

1.7 Outline and Motivation of the Thesis

Due to their porous nature, MOFs are regarded as promising materials for a variety of applications. Since the properties and functionalities of MOFs can be tuned by reaction conditions and the choice of metal centers and ligands, a better understanding of the synthesis process should help provide guidance in improving existing materials and

designing new MOFs. In this thesis, Atomic Force Microscopy (AFM), combined with Powder X-ray diffraction (pXRD) and Scanning Electron Microscopy (SEM), is used to investigate the surface growth of several MOFs. The motivation is to enhance the knowledge of the self-assembly process of these MOFs and optimize the synthesis conditions to better suit the designed needs. In Chapter 2, experimental details and instrumentations used in the thesis are discussed. The third chapter focuses on the investigation of the gallium analog of a flexible MOF known as MIL-53. Ga-MIL-53 was successfully prepared under different reaction conditions, and the growth mechanisms on the surface were discussed. Experiments were also conducted to observe the surface changes after the flexible framework undergoes a phase transition. In chapter 4, three SDB-based MOFs, PbSDB, CaSDB and CdSDB, were investigated using AFM. Since they all use SDB as the organic ligand, their surface features, as well as termination structures, were compared to investigate the effect of metal centers on crystallization.

1.8 References

1. Zhou, H.-C.; Long, J. R.; Yaghi, O. M., Introduction to Metal–Organic Frameworks. *Chemical Reviews* **2012**, *112* (2), 673-674.
2. Furukawa, H.; Cordova, K. E.; O’Keeffe, M.; Yaghi, O. M., The Chemistry and Applications of Metal-Organic Frameworks. *Science* **2013**, *341* (6149).
3. Chae, H. K.; Siberio-Pérez, D. Y.; Kim, J.; Go, Y.; Eddaoudi, M.; Matzger, A. J.; O’keeffe, M.; Yaghi, O. M., A Route to High Surface Area, Porosity and Inclusion of Large Molecules in Crystals. *Nature* **2004**, *427* (6974), 523-527.

4. Getman, R. B.; Bae, Y.-S.; Wilmer, C. E.; Snurr, R. Q., Review and Analysis of Molecular Simulations of Methane, Hydrogen, and Acetylene Storage in Metal–Organic Frameworks. *Chemical reviews* **2011**, *112* (2), 703-723.
5. Sumida, K.; Rogow, D. L.; Mason, J. A.; McDonald, T. M.; Bloch, E. D.; Herm, Z. R.; Bae, T.-H.; Long, J. R., Carbon Dioxide Capture in Metal–Organic Frameworks. *Chemical Reviews* **2011**, *112* (2), 724-781.
6. Suh, M. P.; Park, H. J.; Prasad, T. K.; Lim, D.-W., Hydrogen Storage in Metal–Organic Frameworks. *Chemical Reviews* **2011**, *112* (2), 782-835.
7. Li, J.-R.; Sculley, J.; Zhou, H.-C., Metal–Organic Frameworks for Separations. *Chemical Reviews* **2012**, *112* (2), 869-932.
8. Banerjee, D.; Simon, C. M.; Plonka, A. M.; Motkuri, R. K.; Liu, J.; Chen, X.; Smit, B.; Parise, J. B.; Haranczyk, M.; Thallapally, P. K., Metal-Organic Framework with Optimally Selective Xenon Adsorption and Separation. *Nature Communications* **2016**, *7*, 11831.
9. Horcajada, P.; Gref, R.; Baati, T.; Allan, P. K.; Maurin, G.; Couvreur, P.; Férey, G.; Morris, R. E.; Serre, C., Metal–Organic Frameworks in Biomedicine. *Chemical Reviews* **2012**, *112* (2), 1232-1268.
10. Yoon, M.; Srirambalaji, R.; Kim, K., Homochiral Metal-Organic Frameworks for Asymmetric Heterogeneous Catalysis. *Chemical Reviews* **2011**, *112* (2), 1196-1231.
11. Long, J. R.; Yaghi, O. M., The Pervasive Chemistry of Metal–Organic Frameworks. *Chemical Society Reviews* **2009**, *38* (5), 1213-1214.

12. Stock, N.; Biswas, S., Synthesis of Metal-Organic Frameworks (MOFs): Routes to Various MOF Topologies, Morphologies, and Composites. *Chemical Reviews* **2011**, *112* (2), 933-969.
13. Cook, T. R.; Zheng, Y.-R.; Stang, P. J., Metal-Organic Frameworks and Self-Assembled Supramolecular Coordination Complexes: Comparing and Contrasting the Design, Synthesis, and Functionality of Metal-Organic Materials. *Chemical Reviews* **2012**, *113* (1), 734-777.
14. Yaghi, O. M.; O'keeffe, M.; Ockwig, N. W.; Chae, H. K.; Eddaoudi, M.; Kim, J., Reticular Synthesis and the Design of New Materials. *Nature* **2003**, *423* (6941), 705-714.
15. Loiseau, T.; Serre, C.; Huguenard, C.; Fink, G.; Taulelle, F.; Henry, M.; Bataille, T.; Férey, G., A Rationale for the Large Breathing of the Porous Aluminum Terephthalate (MIL-53) Upon Hydration. *Chemistry—A European Journal* **2004**, *10* (6), 1373-1382.
16. Serre, C.; Millange, F.; Thouvenot, C.; Noguès, M.; Marsolier, G.; Louër, D.; Férey, G., Very Large Breathing Effect in the First Nanoporous Chromium (III)-Based Solids: MIL-53 or $\text{Cr}^{\text{III}}(\text{OH}) \cdot \{\text{O}_2\text{C}-\text{C}_6\text{H}_4-\text{CO}_2\} \cdot \{\text{HO}_2\text{C}-\text{C}_6\text{H}_4-\text{CO}_2\text{H}\}_x \cdot \text{H}_2\text{O}_y$. *Journal of the American Chemical Society* **2002**, *124* (45), 13519-13526.
17. Vougho-Zanda, M.; Huang, J.; Anokhina, E.; Wang, X.; Jacobson, A. J., Tossing and Turning: Guests in the Flexible Frameworks of Metal (III) Dicarboxylates. *Inorganic Chemistry* **2008**, *47* (24), 11535-11542.

18. Whitfield, T. R.; Wang, X.; Liu, L.; Jacobson, A. J., Metal-Organic Frameworks Based on Iron Oxide Octahedral Chains Connected by Benzenedicarboxylate Dianions. *Solid State Sciences* **2005**, 7 (9), 1096-1103.
19. Mowat, J. P.; Seymour, V. R.; Griffin, J. M.; Thompson, S. P.; Slawin, A. M.; Fairen-Jimenez, D.; Düren, T.; Ashbrook, S. E.; Wright, P. A., A Novel Structural Form of MIL-53 Observed for the Scandium Analogue and Its Response to Temperature Variation and CO₂ Adsorption. *Dalton Transactions* **2012**, 41 (14), 3937-3941.
20. Anokhina, E. V.; Vougo-Zanda, M.; Wang, X.; Jacobson, A. J., In (OH) BDC·0.75 BDCH₂ (BDC= Benzenedicarboxylate), a Hybrid Inorganic-Organic Vernier Structure. *Journal of the American Chemical Society* **2005**, 127 (43), 15000-15001.
21. Volkringer, C.; Loiseau, T.; Guillou, N.; Férey, G.; Elkaïm, E.; Vimont, A., XRD and IR Structural Investigations of a Particular Breathing Effect in the MOF-Type Gallium Terephthalate MIL-53 (Ga). *Dalton Transactions* **2009**, (12), 2241-2249.
22. Zhang, Y.; Lucier, B. E.; Huang, Y., Deducing CO₂ Motion, Adsorption Locations and Binding Strengths in a Flexible Metal-Organic Framework without Open Metal Sites. *Physical Chemistry Chemical Physics* **2016**, 18 (12), 8327-8341.
23. Colombo, V.; Montoro, C.; Maspero, A.; Palmisano, G.; Masciocchi, N.; Galli, S.; Barea, E.; Navarro, J. A., Tuning the Adsorption Properties of Isorecticular Pyrazolate-Based Metal-Organic Frameworks through Ligand Modification. *Journal of the American Chemical Society* **2012**, 134 (30), 12830-12843.
24. Chen, T.-H.; Popov, I.; Kaveevivitchai, W.; Miljanić, O. S., Metal-Organic Frameworks: Rise of the Ligands. *Chemistry of Materials* **2014**, 26 (15), 4322-4325.

25. Xuan, W.; Zhu, C.; Liu, Y.; Cui, Y., Mesoporous Metal-Organic Framework Materials. *Chemical Society Reviews* **2012**, *41* (5), 1677-1695.
26. Eddaoudi, M.; Kim, J.; Rosi, N.; Vodak, D.; Wachter, J.; O'keeffe, M.; Yaghi, O. M., Systematic Design of Pore Size and Functionality in Isorecticular MOFs and Their Application in Methane Storage. *Science* **2002**, *295* (5554), 469-472.
27. Makal, T. A.; Wang, X.; Zhou, H.-C., Tuning the Moisture and Thermal Stability of Metal–Organic Frameworks through Incorporation of Pendant Hydrophobic Groups. *Crystal Growth & Design* **2013**, *13* (11), 4760-4768.
28. Sunagawa, I., *Crystals : Growth, Morphology, and Perfection*. Cambridge University Press: Cambridge, 2005.
29. Cejka, J.; Corma, A.; Zones, S., *Zeolites and Catalysis: Synthesis, Reactions and Applications*. John Wiley & Sons: 2010.
30. Hammond, C.; Hammond, C., *Basics of Crystallography and Diffraction*. Oxford: 2001.
31. Bishop, A. C., *An Outline of Crystal Morphology*. Hutchinson Scientific and Technical: London, 1967.
32. Seager, A.; Davidson, W., Changes in Habit During the Growth of Baryte Crystals from the North of England. *Mineralogical Magazine* **1952**, *29*, 885-894.
33. Harker, D., A New Law of Crystal Morphology, Extending the Law of Bravais. *American Mineralogist* **1937**, *22*, 446-467.
34. Widlak, N.; Hartel, R. W.; Narine, S., *Crystallization and Solidification Properties of Lipids*. The American Oil Chemists Society: 2001.
35. Eaton, P.; West, P., *Atomic Force Microscopy*. Oxford University Press: 2010.

36. Shöâèè, M.; Agger, J. R.; Anderson, M. W.; Attfield, M. P., Crystal Form, Defects and Growth of the Metal Organic Framework HKUST-1 Revealed by Atomic Force Microscopy. *CrystEngComm* **2008**, *10* (6), 646-648.
37. Moh, P. Y.; Cubillas, P.; Anderson, M. W.; Attfield, M. P., Revelation of the Molecular Assembly of the Nanoporous Metal Organic Framework ZIF-8. *Journal of the American Chemical Society* **2011**, *133* (34), 13304-13307.

Chapter 2

2 Experimental

2.1 MOF Sample Preparation

As mentioned in the previous chapter, synthesis methods for MOFs are very diverse. Each of them has unique strengths and weaknesses depending on the purposes of experimentations. For our surface studies utilizing AFM, large single crystals (i.e. optimally greater than 20 μm in all dimensions) with flat surfaces are strongly preferred for good-quality AFM measurements. In this thesis, the hydrothermal method is the only synthesis method used since all MOFs studied are originally reported to be prepared using this method.¹⁻⁵ Additionally, hydrothermal synthesis is capable of producing large single crystals that are suitable for AFM observations.

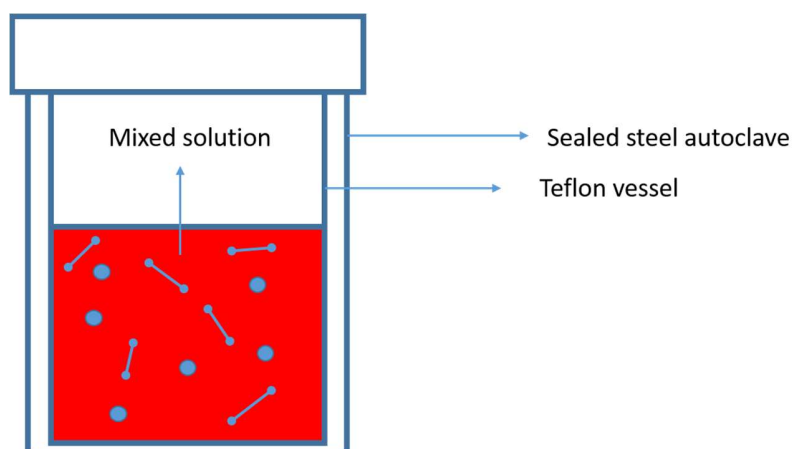


Figure 2-1 Scheme showing the set-up of a hydrothermal synthesis.

The synthesis is started by mixing the metal salt and the precursor of the linker with solvent in a Teflon-built vessel. The mixture is stirred to achieve the homogeneity of all species. The container is then transported to a sealed steel autoclave and heated in an oven. The temperature will be kept constant for a certain duration of time, depending on the particular

MOF being synthesized. After that, the autoclave will be taken out of the oven and reaction system is allowed to cool to room temperature. MOF crystals as products will be collected either by vacuum filtration or centrifugation.

2.2 Characterization Methods

Multiple techniques were used to characterize the synthesized MOFs. Powder X-ray diffraction experiments were firstly conducted to verify the purity and crystallinity of the product. Then Scanning Electron Microscopy in combination with BFDH theoretical calculations was employed to identify major faces present in the crystal habit. After the faces have been indexed, Atomic Force Microscopy was used to make surface observations. The fundamental principles and technical details of those methods will be discussed in the following sections.

2.2.1 Atomic Force Microscopy

AFM observations were made using a Park Systems XE-100 Atomic Force Microscope. A cantilever with a nominal spring constant of 40 N/m, resonant frequency of 300 kHz was used, and the tip has a radius of 10 nm. Calibration grating (Model TGZ1_PTB) obtained from NT-MDT was used for Z-axis calibration before measurements were conducted. The grating is made from SiO₂ and has a step height of 21.9±0.8 nm. All the measurements were conducted in air at room temperature under the dynamic force mode. Under this mode, the cantilever oscillates around a particular frequency, which will be manually determined by the user before a measurement is taken. Ideally, the frequency should be as close to the cantilever's own resonance frequency as possible to give the best image quality. The amplitude (set point) of the oscillation will also be determined which will decide the

distance and applied force between the tip and the surface. There is no empirical number for the set point, as it will depend on multiple factors such as the nature of the surface scanned and the conditions of the tip. To obtain images with optimal quality, this parameter will be optimized several times before a full scan is conducted. The scan rate varies from 0.5 Hz to 1 Hz depending on the scale of the image. Generally, if the scan rate is high, the risk is that as the tip moves over the sample, there would be less time than required for the feedback system to follow up. As a result, non-optimized scan rate may lead to the loss of surface details.⁶ In our AFM measurements, a fast scan rate of 1 Hz will generally be used for square images with their edge less than 15 μm . In cases where the regions captured are larger (i.e. $> 15 \times 15 \mu\text{m}^2$) or a notable decrease in image quality is observed, a slower scan rate of 0.5 Hz will be used.

As a surface technique, AFM requires the sample to be fixed during scanning. This means that when MOF crystals physically contact with the AFM tip during the scan, their movement must be avoided. In our sample preparation, square aluminum plates were used to mount the single crystals. Prior to use, the top surface of the aluminum plates will be covered by double-sided tape. Then subject crystals will be dispersively transferred onto the sticky surface using a needle. Following that, the crystals will be further stabilized by the application of pressurized air. The whole setup is described in Figure 2-2.

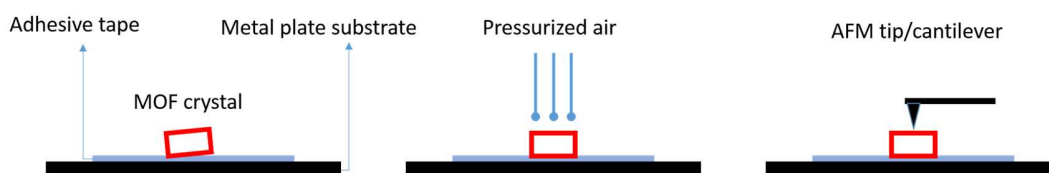


Figure 2-2 Schemes showing the sample preparation process.

The XEI image process software package was used to perform AFM data analysis. In the experiments conducted in this thesis, two types of images were collected and processed: error (deflection) images and topography images. The error image records the deflection of the cantilever as it encounters surface topologies. Such a deflection can be regarded as an “error” as it will cause the amplitude of the oscillation to drift from its set point, and it will be “corrected” by the feedback system as the scan continues. Despite the fact that error images do not contain any height information, they will be displayed as good reflections of surface morphologies. On the other hand, cross-sectional graphs are generated using the height information derived from topography images. When the surface is tilted (in most cases it will), leveling/flattening treatment is conducted before a height is measured.

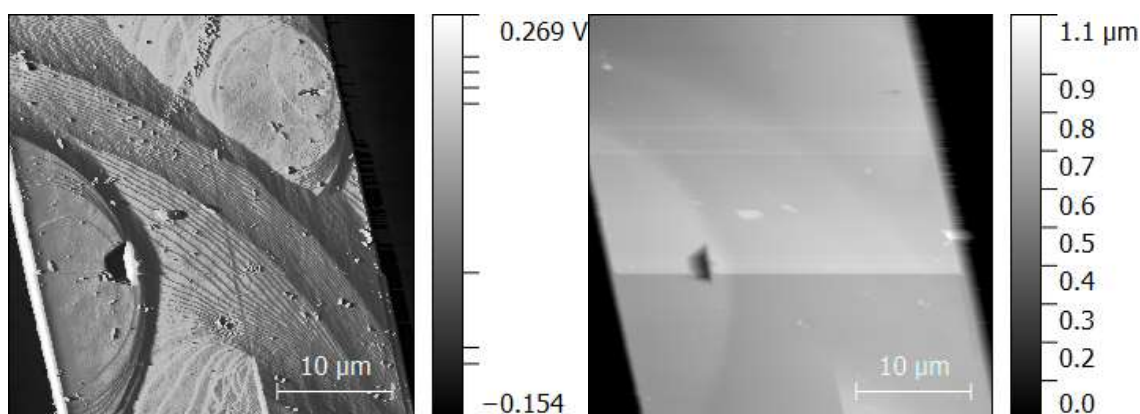


Figure 2-3 Comparison between an error image (Left) and a topography image (Right). The two images feature the same region of a MOF crystal. Those images are processed using Gwyddion software.

2.2.2 Powder X-ray Diffraction

Before the crystals are taken to AFM for surface observations, it is firstly essential to confirm their purity and crystallinity. To fulfill that purpose, powder X-ray diffraction will be used. This technique could probe the long range ordering of crystalline materials by

recording the intensity of X-rays as they are diffracted by the crystal lattice. The diffraction behaviors of the incident beam satisfy the relationship known as the Bragg's law:

$$n\lambda = 2d \sin\theta$$

where λ is the wavelength of the incident beam, d is the interplanar spacing of the crystallographic plane and θ is the diffraction angle. The intensities can be plotted with 2θ , and the resulting patterns will be compared with calculated patterns for identification purposes.

In this thesis, an Inel CPS Powder Diffractometer with a Cu K α radiation ($\lambda = 1.5406 \text{ \AA}$) was used to acquire pXRD patterns for routine characterization in the 2θ range of 5-120°.

2.2.3 Scanning Electron Microscopy

Scanning electron micrographs were captured to identify the habit of synthesized crystals and aid the index of the main faces. In this thesis, related experiments were conducted using an LEO (Zeiss) 1540XB FIB/SEM instrument.

2.3 References

1. Vougo-Zanda, M.; Huang, J.; Anokhina, E.; Wang, X.; Jacobson, A. J., Tossing and Turning: Guests in the Flexible Frameworks of Metal (III) Dicarboxylates. *Inorganic Chemistry* **2008**, 47 (24), 11535-11542.
2. Zhang, Y.; Lucier, B. E.; Huang, Y., Deducing CO₂ Motion, Adsorption Locations and Binding Strengths in a Flexible Metal-Organic Framework without Open Metal Sites. *Physical Chemistry Chemical Physics* **2016**, 18 (12), 8327-8341.

3. Lin, J.-D.; Wu, S.-T.; Li, Z.-H.; Du, S.-W., A Series of Novel Pb (II) or Pb (II)/M (II)(M= Ca and Sr) Hybrid Inorganic–Organic Frameworks Based on Polycarboxylic Acids with Diverse Pb–O–M (M= Pb, Ca and Sr) Inorganic Connectivities. *CrystEngComm* **2010**, *12* (12), 4252-4262.
4. Banerjee, D.; Zhang, Z.; Plonka, A. M.; Li, J.; Parise, J. B., A Calcium Coordination Framework Having Permanent Porosity and High CO₂/N₂ Selectivity. *Crystal Growth & Design* **2012**, *12* (5), 2162-2165.
5. Plonka, A. M.; Banerjee, D.; Woerner, W. R.; Zhang, Z.; Li, J.; Parise, J. B., Effect of Ligand Geometry on Selective Gas-Adsorption: The Case of a Microporous Cadmium Metal–Organic Framework with a V-Shaped Linker. *Chemical Communications* **2013**, *49* (63), 7055-7057.
6. Eaton, P.; West, P., *Atomic Force Microscopy*. Oxford University Press: New York, 2010.

Chapter 3

3 An Investigation of Crystal Growth of Metal-Organic Framework Ga-MIL-53

3.1 Introduction

M-MIL-53 (M= Al, Cr, Ga) is a series of MOFs that is capable of gas absorption such as carbon dioxide and has been studied using various methods such as solid-state NMR and simulation.¹⁻² The second building unit is an octahedral $\text{MO}_4(\text{OH})_2$ where four oxygens come from the benzenedicarboxylate (BDC) ligands and the other two come from bridging hydroxyl groups between the metals. This MOF has a flexible network that can change the size of its channel to accommodate different guest molecules inside. Such a phenomenon is referred to as “breathing effect”.³⁻⁵ The ability to accommodate guest molecules within their frameworks has made Ga-MIL-53 a promising subject for AFM crystallization studies, and it motivates us to explore its self-assembly process as well as surface features.

The habit and morphology of crystals are dependent not only on the internal symmetry but also on the crystallization conditions. The crystallization of single crystals is affected by other synthesis parameters such as reaction time, the degree of supersaturation and metal to ligand ratio. Thus single crystals of Ga-MIL-53 were prepared to explore crystal growth under different conditions.

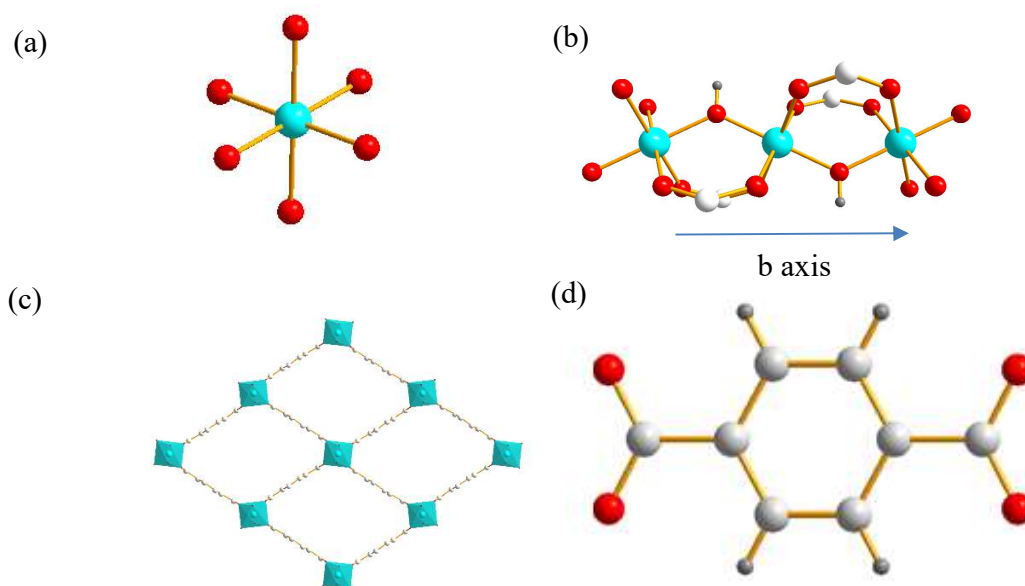


Figure 3-1 (a) shows the octahedral $\text{MO}_4(\text{OH})_2$ secondary building unit; (b) shows the chain formed along b axis. A rhombus channel along b axis is demonstrated in (c). (d) shows the structure of the benzenedicarboxylate linker.

3.2 Experimental

3.2.1 Sample Preparation

All samples were prepared according to references with slight modifications² and all reagents and solvents used were purchased from Sigma-Aldrich. In the preparation of Ga-MIL-53, $\text{Ga}(\text{NO}_3)_3 \cdot \text{H}_2\text{O}$, benzene-1,4-dicarboxylic acid (BDCA) and deionized water were mixed in a stainless steel autoclave and heated at 200 °C. A typical literature synthesis lasts 3 days. Colorless parallelepiped single crystals were recovered and collected. Before further characterizations, the product was washed with DMF to remove unreacted ligand crystals. Detailed reaction stoichiometry for experiments performed is summarized in Table 3-1.

Table 3-1 Summary of synthesis conditions used in successful attempts.

Experiment	Gallium Nitrate (mol/L)	BDCA (mol/L)	Solvent (mL)	Synthesis time (day)	Molar ratio (Ga:BDCA)
A	0.1	0.2	10	0.5	1:2
B	0.1	0.2	10	1	1:2
C	0.1	0.2	10	2	1:2
D	0.1	0.2	10	3	1:2
E	0.1	0.2	10	4	1:2
F	0.1	0.1	10	3	1:1
G	0.1	0.15	10	3	1:1.5
H	0.1	0.175	10	3	1:1.75
I	0.2	0.2	10	3	1:1
J	0.05	0.1	20	3	1:2

3.2.2 Characterization

AFM measurements. AFM observations were made using a Park Systems XE-100 Atomic Force Microscope. ~~Square aluminum plates were used to place the single crystals. To eliminate the movement of sample crystals during the scan when they physically contact with the AFM tip, adhesive tapes were attached to the surface of the plates before sample application. All the measurements were conducted under the dynamic force mode in air at room temperature. A cantilever with a nominal spring constant of 40 N/m, resonant frequency of 300 kHz is used, and the tip has a radius of 10 nm. The scan rate varies from 0.5 Hz to 1 Hz depending on the scale of the image; generally slower scan rate is used for~~

~~larger images to obtain optimum image quality.~~ The XEI image process software package was used to perform image flattening and height analysis.

X-ray Diffraction. An Inel CPS Powder Diffractometer with a Cu K α radiation ($\lambda = 1.5406$ Å) were used to obtain pXRD patterns for routine characterization in the 2θ range of 5-120°.

Habit prediction. Relative surface areas for dominant crystallographic planes were calculated using the built in BFDH calculation function of the Mercury software.

SEM. All Scanning electron micrographs were captured using a LEO (Zeiss) 1540XB FIB/SEM instrument.

3.3 Results and Discussion

3.3.1 Surface Observation on {101} face

Single crystals of MIL-53 (Ga) were successfully prepared by hydrothermal synthesis. The as-made orthorhombic single crystals were obtained and they have a uniform shape of parallelepiped with a size of 100-300 μm in length, which is consistent with the observation from Volkringer *et al.*⁶ The shape that a crystal could develop is called the crystal habit, which can be described by sets of crystal faces that are related by symmetry known as crystal forms.⁷ In our AFM studies, to correlate the heights of the observed nano-scaled surface features with the crystal structure, the Miller indices of the crystallographic planes where the AFM tip is landed must be known. Unfortunately, no previous work could be found regarding face assignation for these MOFs. Attempts to index the faces with single crystal XRD experiments were made but they were unsuccessful. However, we were able to predict the crystal habits by employing the BFDH method.⁸ The method is named after

Bravais, Frediel, Donney and Parker, which assumes that the slowest growing faces are the ones with the longest inter-planar distance. The relationship is defined as

$$R_{hkl} \propto 1/d_{hkl}$$

where R_{hkl} is the growth rate of a crystallographic plane denoted as hkl in the direction that perpendicular to the surface and d_{hkl} is the corresponding inter-planar spacing. Since faces that grow faster will disappear first, the most predominant faces are those with the longest inter-planar spacing. Besides that, the method also takes the extinction conditions of the space group into account and has been found to give reasonable predictions confirmed by experimental observations.⁹

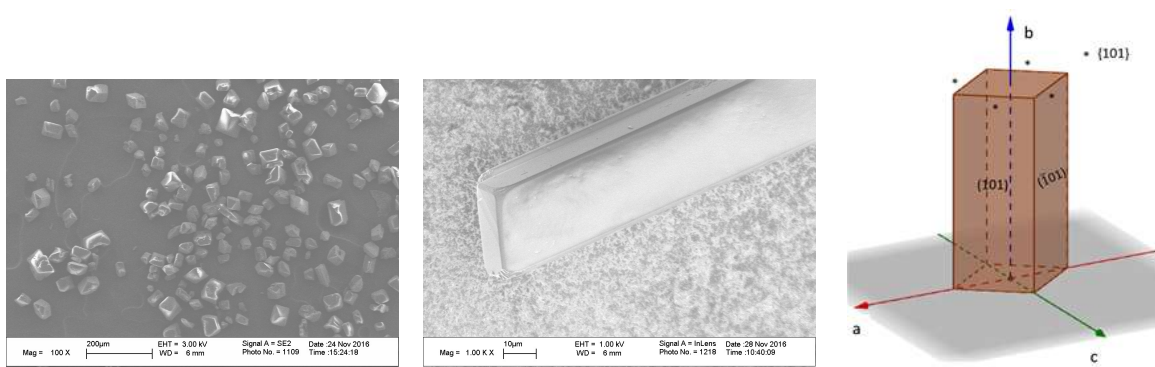


Figure 3-2 (Left) An overview of Ga-MIL-53 single crystals from SEM. (Middle) A zoomed in SEM micrograph featuring one single Ga-MIL-53 crystal. (Right) Scheme showing habit prediction.

The as-made crystal has the orthorhombic $Pnma$ space group. The framework has a rhombus channel along the b axis that is occupied by excess BDCA molecules. BFDH calculation shows that the crystal surface is mainly covered by $\{101\}$ facets which are responsible for 53.2% of the total facet area. Second to the $\{101\}$ facets are the $\{200\}$ facets covering only 16.8% of the total facet area (Figure 3-2). From SEM micrographs,

only four major rectangular faces can be identified. Based on the prediction, they are assigned as $\{101\}$ and this four-faced open form is parallel to the b axis (Figure 3-2).

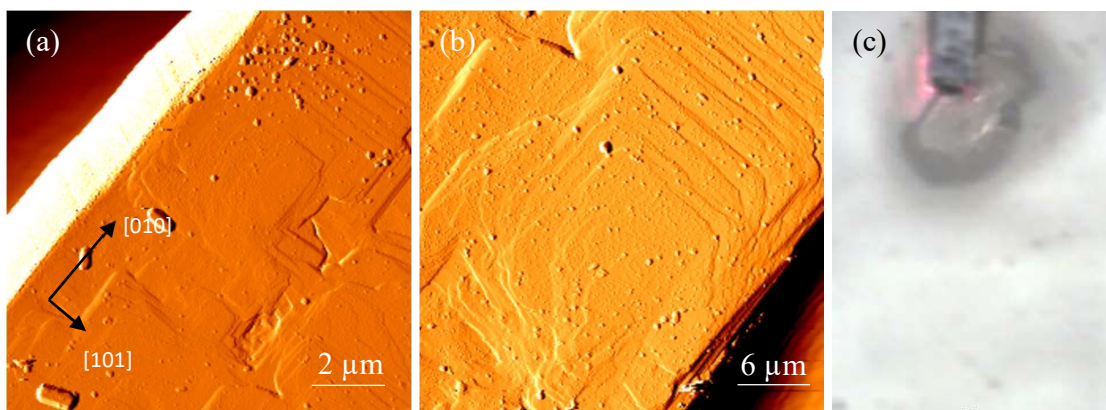


Figure 3-3 (a-b) AFM error images of Ga-MIL-53 after 3 days of synthesis; (c) optical image showing the single crystal that was being scanned.

The growth behaviors of Ga-MIL-53 crystals were investigated using *ex-situ* AFM. Examples of the observations on the $\{101\}$ faces are shown in Figures 3-3. The three images feature the same single crystal. It can be seen that the growth follows the “birth and spread” crystal growth mechanism, with layered hillocks exhibiting a rectangular morphology. The steps parallel to $[010]$ direction are much longer compared with steps parallel to $[101]$ direction, indicating the much faster growth along the former direction. Terraces are flat, suggesting a strong preference for the surface termination.

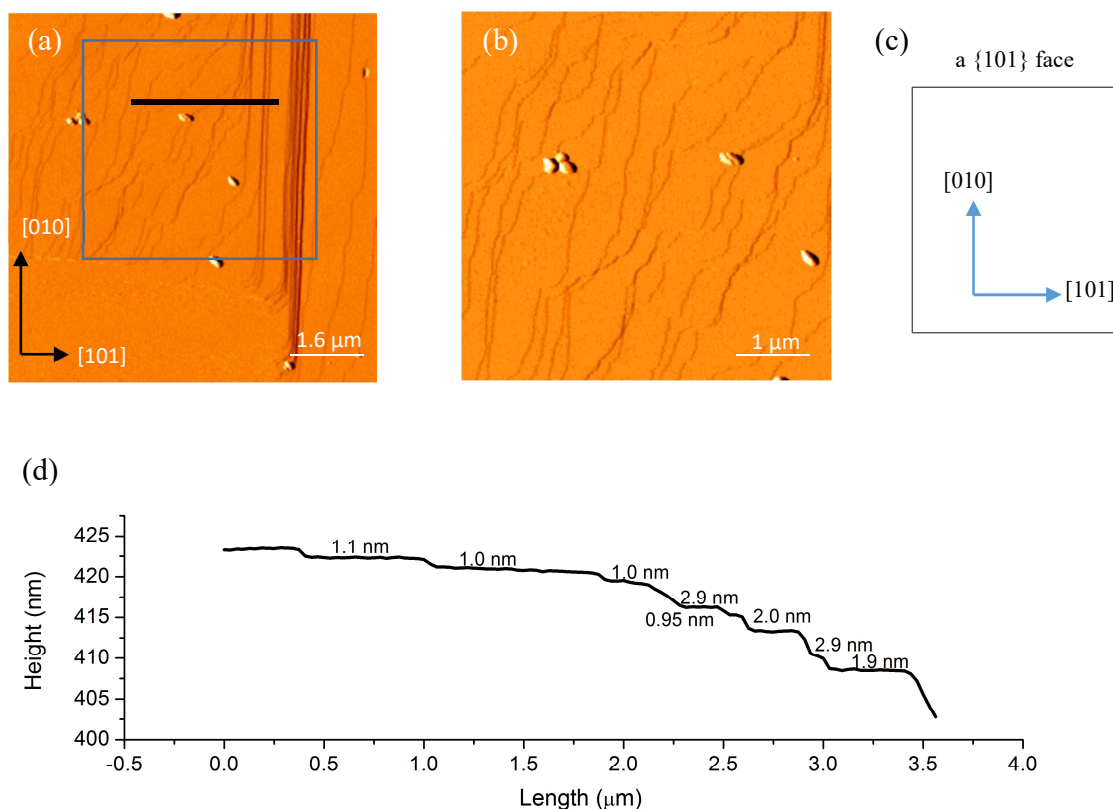


Figure 3-4 AFM error images of Ga-MIL-53 after 3 days of synthesis; (a) a growth hillock on a {101} face; (b) zoomed in image showing the area enclosed in the box on (a). (c) describes the orientation of the {101} face studied and (d) shows the height profile acquired along the line in (a).

Height analysis on the AFM image (Figure 3-4) reveals that the smallest steps have a height of 1.0 ± 0.1 nm which corresponds to the d_{101} crystal spacing. Steps with a height of 2.0 nm and 3.0 nm were also observed which are the multiples of the d_{101} spacing.

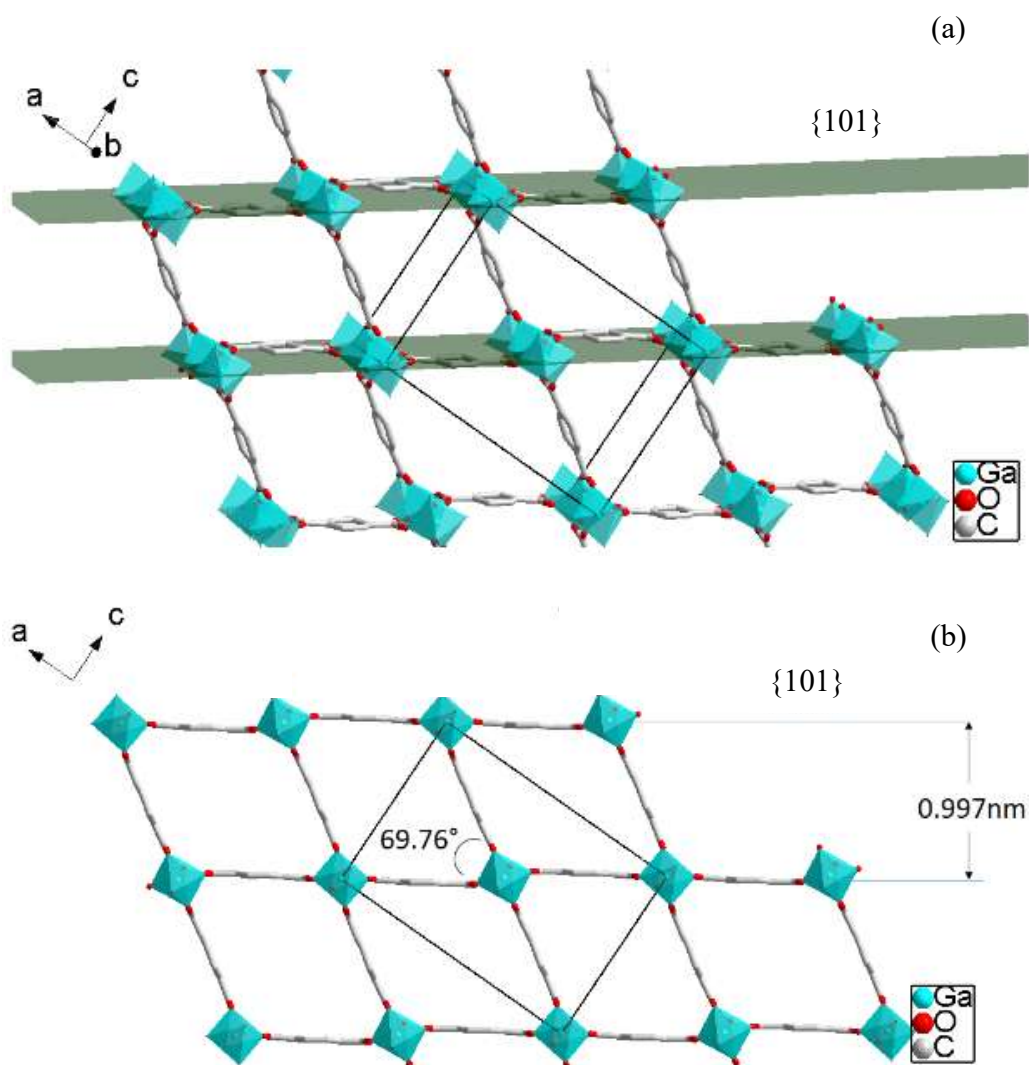


Figure 3-5 The MIL-53(Ga) structure viewing through the rhombus channel. Hydrogen atoms are omitted for clarity.

From Figure 3-5 it can be seen that the $\{101\}$ faces grow by the addition of Ga-centred octahedra bridged by benzenedicarboxylate ligands to form rhombus channels along the b axis. Here we propose possible termination layers that are responsible for the 0.97 nm d_{101} spacing without the breaking of the intramolecular bonds within the benzenedicarboxylate ligand. The surface could either terminate with a layer of Ga-centred octahedra linked by horizontal benzenedicarboxylate ligands (Figure 3-5b), or solely with a layer of benzenedicarboxylate ligands. (Figure 3-5a). If the termination species are the

benzenedicarboxylate ligands, in order to form a consistent step of 0.9 nm they would have to maintain the angle of 69.76° between themselves and the plane beneath them, which is less likely to happen since only one end of the ligands is incorporated into the framework. Thus, it is inferred that the surface of Ga-MIL-53 is terminated with Ga ions, which is consistent with other studies on zeolites and MOFs showing that the stable termination structures are closed cages.¹⁰⁻¹²

Successive observations on Ga-MIL-53 with different crystallization times have confirmed that the “birth and spread” mechanism is the primary growth mechanism on the {101} surface, where growth occurs through 2D nucleation followed by 2D spreading of the layers. The set of AFM micrographs shown in Figure 3-6 was captured from the {101} surface of a single crystal in a 1-day synthesis batch, which probes growth following the “spiral” mechanism. The growth spiral also developed a rectangular shape. A etch pit was observed at the dislocation center. The strain field present at dislocation sites make them more vulnerable to etching, thus the pit is most likely caused by the dissolution during the post-synthesis process.¹³ Height measurements conducted over the spiral steps revealed that the Burger’s vector of the dislocation is 1.0 nm, corresponds to the height of one monolayer. It is the only occasion that a growth spiral was observed. Still, it indicates that Ga-MIL-53 could grow through the spiral growth mechanism.

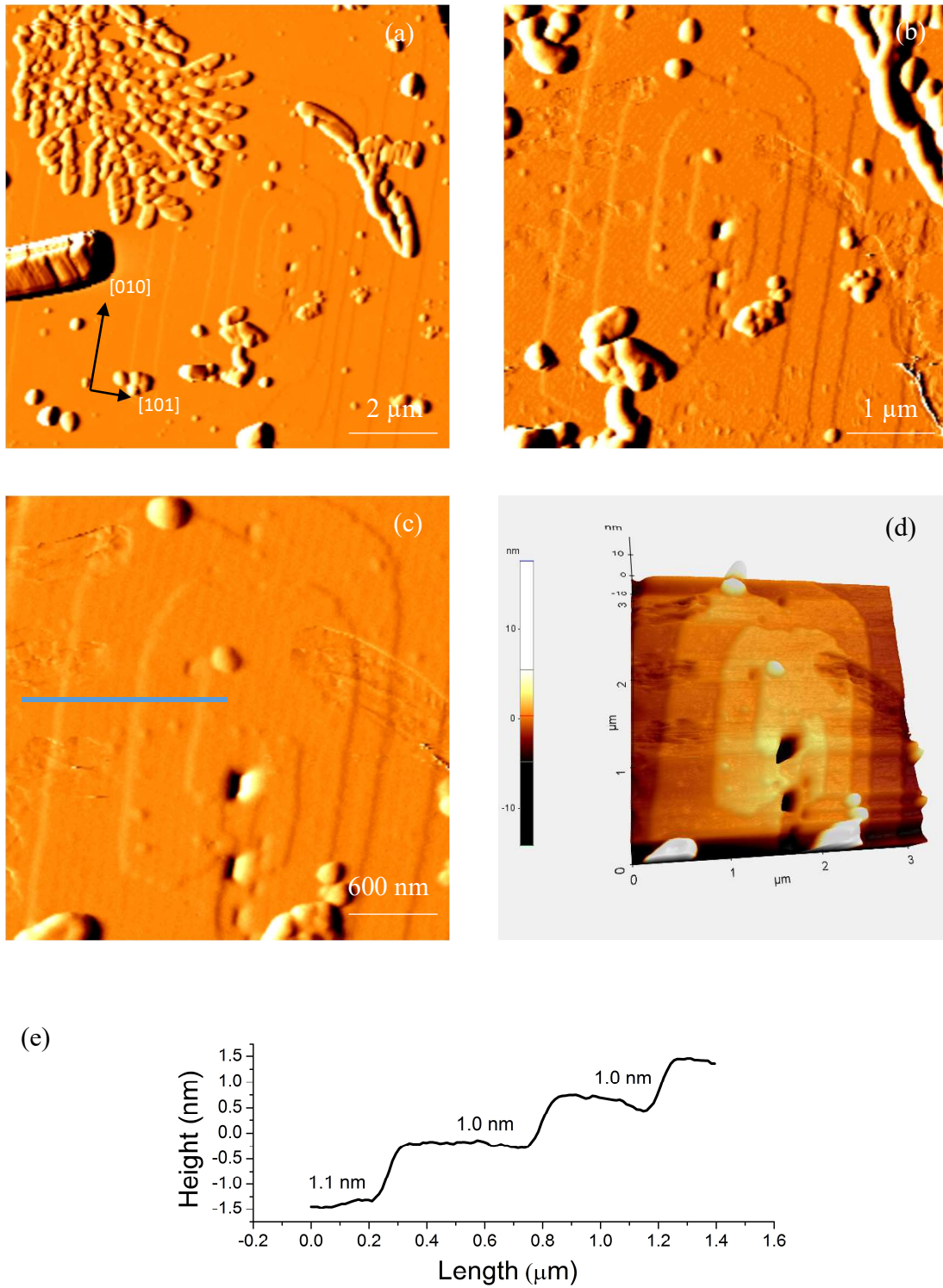


Figure 3-6 (a-c) Error images showing a spiral growth hillock at different scales. (d) A 3D representation of the spiral growth hillock. (e) Height profile along the blue line in c.

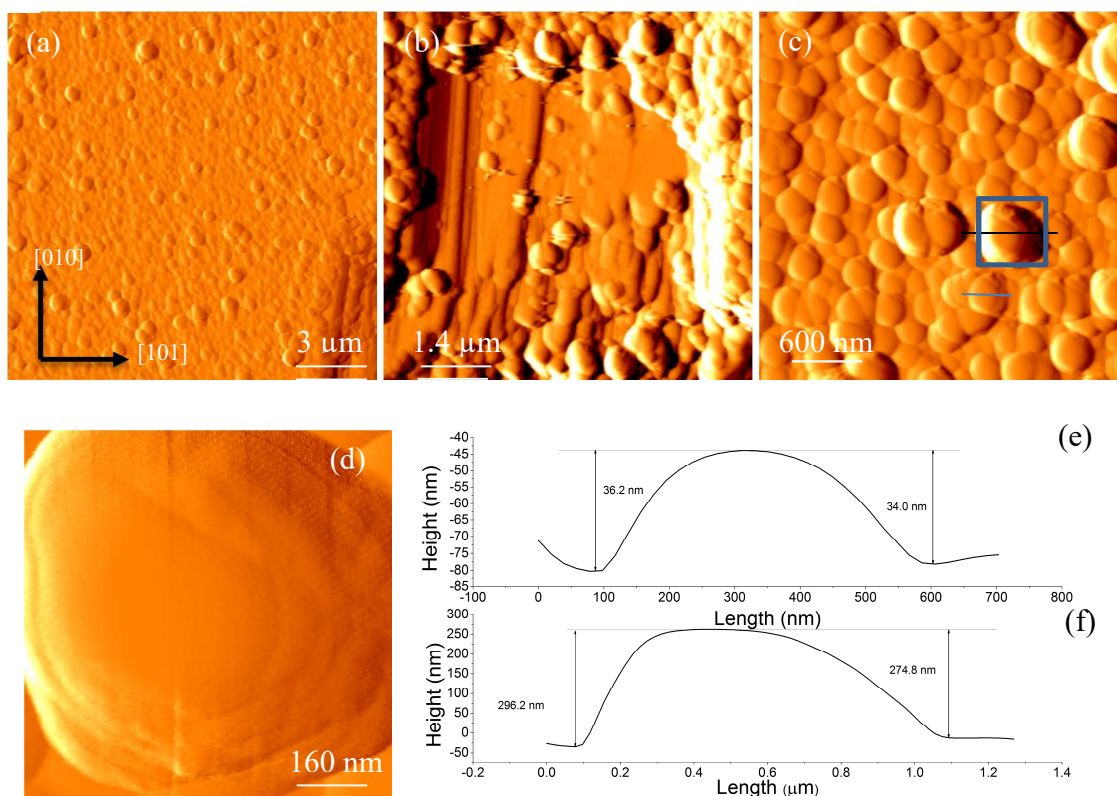


Figure 3-7 AFM deflection images of $\{101\}$ face after re-grown treatment. (d) is the zoom in image of the blue box in (c). (e) and (f) are height profiles measured along the blue line and black line in (c), respectively.

In some studies, synthesized crystals were put back into different growth solutions to re-grow for further AFM observations.^{10, 14-15} When a more diluted growth solution is used, the slower growth rate allows the observation of surface features under lower supersaturation conditions. Here we regrow seed Ga-MIL-53 crystals in a 5% growth solution diluted with water at 200 °C for 3 hours. Figure 3-7 shows the surface of a $\{101\}$ face after re-growth treatment. It can be seen that the surface is covered by a lot of nuclei. Nuclei size ranges from 400 nm to 800 nm in lateral and 20 to 200 nm in height. No nucleus with the 1 nm height is observed, suggesting that the nuclei are stacked with tens and hundreds of layers of the growth unit layer with the height of d_{101} . A zoomed in image of

nuclei is shown in Figure 3-7d, revealing more details on the surface. It can be seen that the nuclei are actually made from the stacking of many irregular terraces, following the “birth and spread” mechanism. The large amount of nuclei on the plane suggests that even though the growth solution was diluted, it was still supersaturated and the driving force was large enough to surpass the energy barrier required for 2-D nucleation on the surfaces. The nuclei adopt round terraces instead of rectangular, which might be due to the drop of growth anisotropy as the degree of supersaturation decreases. However, the height of individual layers cannot be obtained from the height profile shown in Figure 3-7f. Careful analyses revealed that this is caused by the fact that the width of the terraces is close to or smaller than 20 nm, which is the diameter of the AFM tip used. In this case, the step heights of the terraces cannot be fully resolved. When the tip apex is over the surface of a terrace, the side wall of the tip still touches the edge of an adjacent higher terrace, thus preventing the tip apex from reaching the rest part of the surface. This geometric convolution between the mechanical probe and the surface features of the specimen is known as tip effect, limiting spatial resolutions.¹⁶

It can be concluded that for Ga-MIL-53, growth rate along different crystallographic directions will be influenced by the degree of supersaturation. This is reflected in the round shaped steps observed in the re-grown sample.

3.3.2 Crystal Growth of Ga-MIL-53 at Different Length of Time

All the MOFs in this section were synthesized with a metal: ligand ratio of 1:2 at 200 °C and 10 mL water as solvent. Products from 0.5, 1, 2, 3 and 4 days were all confirmed by PXRD experiment and their patterns are in good agreement with crystallite Ga-MIL-53 reported in the literature (Figure 3-8).

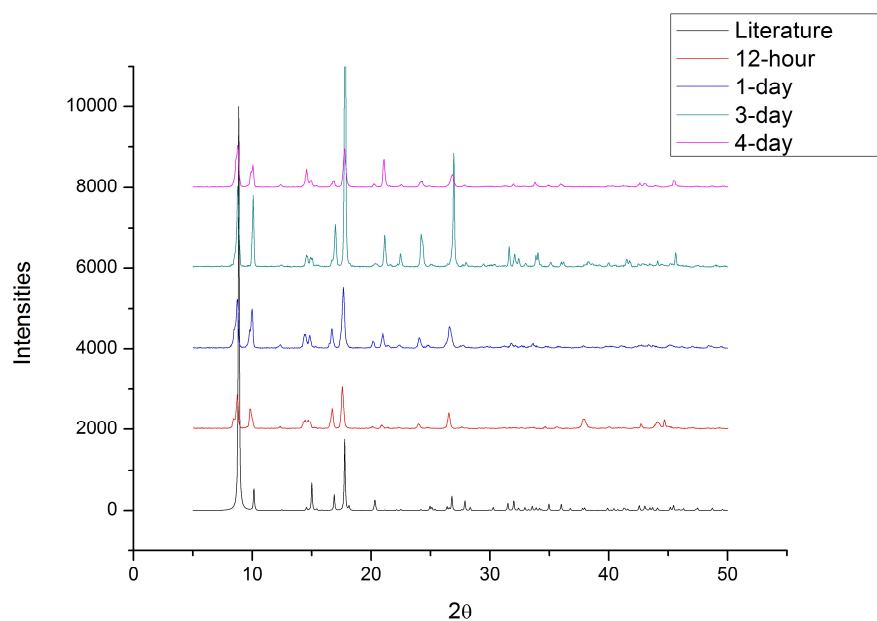


Figure 3-8 Powder X-ray diffraction patterns for Ga-MIL-53 crystallites with different synthesis times.

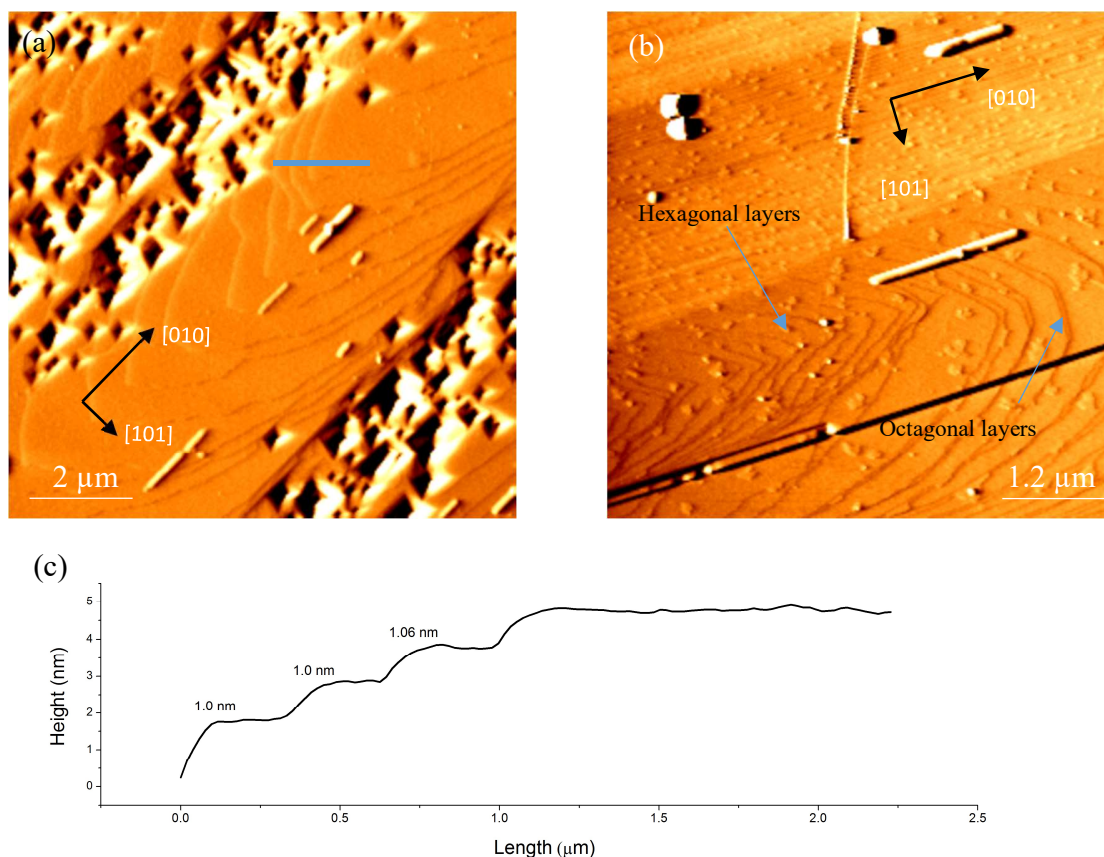


Figure 3-9 (a-b) Error images captured on samples with 1 day synthesis time. (c) Height profile captured along the blue line in (a).

The syntheses of Ga-MIL-53 samples were repeated several times. In each synthesis batch, multiple single crystals were always examined to ensure the universality and reliability of the results. Surface examination on the $\{101\}$ surface of the samples with shorter synthesis time (i.e. 12-hour and 1-day) shows that the growth still followed the “birth and spread” mechanism. Two AFM deflection images captured from 1-day samples are shown in Figure 3-9. Terraces are more extended along $[010]$ direction than $[101]$ direction, suggesting a more rapid growth along the former direction than the latter. The shape of terraces developed were rather different from the rectangular shaped growth hillocks seen on 3-day samples that were discussed previously (Figure 3-3). Instead, a flattened hexagon shape

that tapers along the $[010]$ axis on either end can be observed (Figure 3-9a). In some cases, a transition of shape from hexagonal to rectangle can also be seen on the bottom layers, resulting in an intermediate octagonal shape (Figure 3-9b). In comparison, for the $\{101\}$ surfaces that have crystallized for three days, non-rectangular terraces were rare and their presence was limited in the very top layers (Figure 3-4). Height measurements were conducted across the layers. It is found that even though the terrace shapes are different, the unit layers still possess the height of 1.0 nm, which corresponds to the height of a tilted BDC ligand plus a gallium ion, as discussed previously.

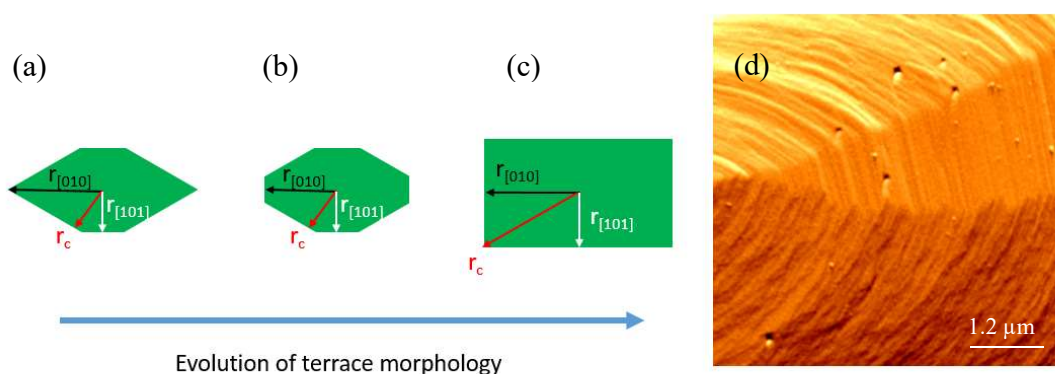


Figure 3-10 (a-c) Schemes showing relationships between growth rates in different terrace morphologies. (d) a layered hillock indicating the transition from hexagonal to rectangular.

Based on the observed terrace morphologies, here we propose a mechanism for layer spreading on $\{101\}$. The relationship between relative spread rate and resulting terrace morphologies is described in Figure 3-10, where the side edges move along the direction labeled as c . In the first stage, terraces formed adopt the hexagonal shape, which was caused by the anisotropic 2-dimensional spreading along different directions. In this case, growth would be fastest along $[010]$ direction and slowest along $[101]$ (Figure 3-10a). As the steps

continued to spread, step edges along $[101]$ started to show up. For that to occur, the step advancement along $[010]$ gradually slowed down, as illustrated in Figure 3-10b. As a result, side edges would vanish in a gradual manner, and a transition from hexagonal-shaped to octagon-shaped terraces was observed. If more synthesis time was allotted (i.e. 3 days), the terraces finally develop into the rectangular shape (Figure 3-10c). These findings suggest that the relative growth rates along different crystallographic directions may change before product crystallization is complete.

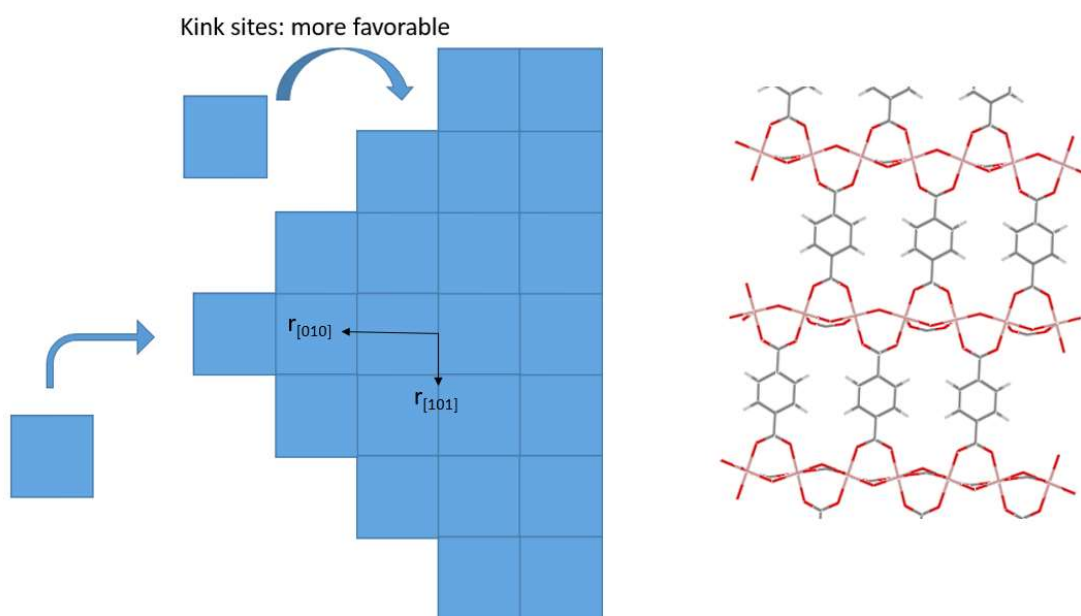


Figure 3-11 (Left) 2-D representation of a $\{101\}$ layer using a Kossel model, where growth units are described as squares. (Right) Schematic representation of a single $\{101\}$ layer which composes of Ga-O-Ga inorganic chain along $[010]$ bridged by BDC linkers along $[101]$.

Figure 3-11 shows that the growth along $[010]$ is achieved by the elongation of Ga-O-Ga inorganic chain, while the layer spreading along the $[101]$ direction requires the incorporation of BDC ligands to bridge the chains. The longer terrace along $[010]$ than that

along [101] may suggest that it is faster to form the Ga-O-Ga inorganic chains than crosslinking them. Physical bonds along [101] and [010] are the only two types of bond chains that exist on the {101} planes. This suggests that the advancement of the side edge (r_c) is just a result of combined growth that occurs along both [101] and [010] directions. The Kossel model predicts that the growth rate normal to the side edge should be faster than the growth rate along [010] and [101] due to the higher kink density along the terrace step.^{13, 17} However, ~~differently as mentioned above~~, initially it was the growth rate along [010] that was faster, but the relationship is reversed as the layer spreads. The change in growth anisotropy could be induced by multiple variables, such as temperature, pressure, and degree of supersaturation.^{11, 14, 18-19} However, it is less likely that those factors are responsible for the change of relative growth rates, because the layers with different morphologies were developed on the same surface. One possible explanation is that initially the species have a lower diffusion rate to the kinked sites, and the inhibition later vanishes as the layers spread. However, more detailed analysis on the evolution of the terraces would require further experimentation.

3.3.3 Crystal Growth of Ga-MIL-53 with different Ga:BDCA ratio

Previous studies on MOF-5 have revealed that terraces could develop into different morphologies when metal:ligand ratio was changed.¹⁴ In our previous synthesis of Ga-MIL-53, a Ga:BDCA ratio of 1:2 was used. In this section, several experiments were conducted to investigate whether similar effects exist in the crystallization of Ga-MIL-53.

Under literature conditions, the amount of BDCA used is in excess due to two reasons; the formula suggests that in the framework Ga and BDCA has a 1:1 relationship and the solid product collected from synthesis consists of a large proportion of unreacted needle-shaped

BDCA crystals. Thus firstly the Ga:BDCA ratio of 1:1 was chosen to study its potential effect on crystallization. The 1:1 ratio can be achieved in two ways, either by increasing the amount of Ga species used, as in experiment I, or by decreasing the amount of BDCA ligand used, as in experiment F.

Figure 3-12a shows the $\{101\}$ growth images taken after 3 day synthesis with a 1:1 Ga:BDCA ratio. It can be observed that the terraces have the shape of distorted hexagon. In comparison, for the 1:2 samples also with the full 3 day synthesis, rectangle is the dominate form for growth hillocks despite the occasional presence of hexagonal shaped layers at the top. Height measurements show an average height of 1.0 nm for the hexagonal monolayers, which is consistent with previous measurements. This signifies that varying the Ga:BDCA ratio from 1:2 to 1:1 does not change the $\{101\}$ surface termination.

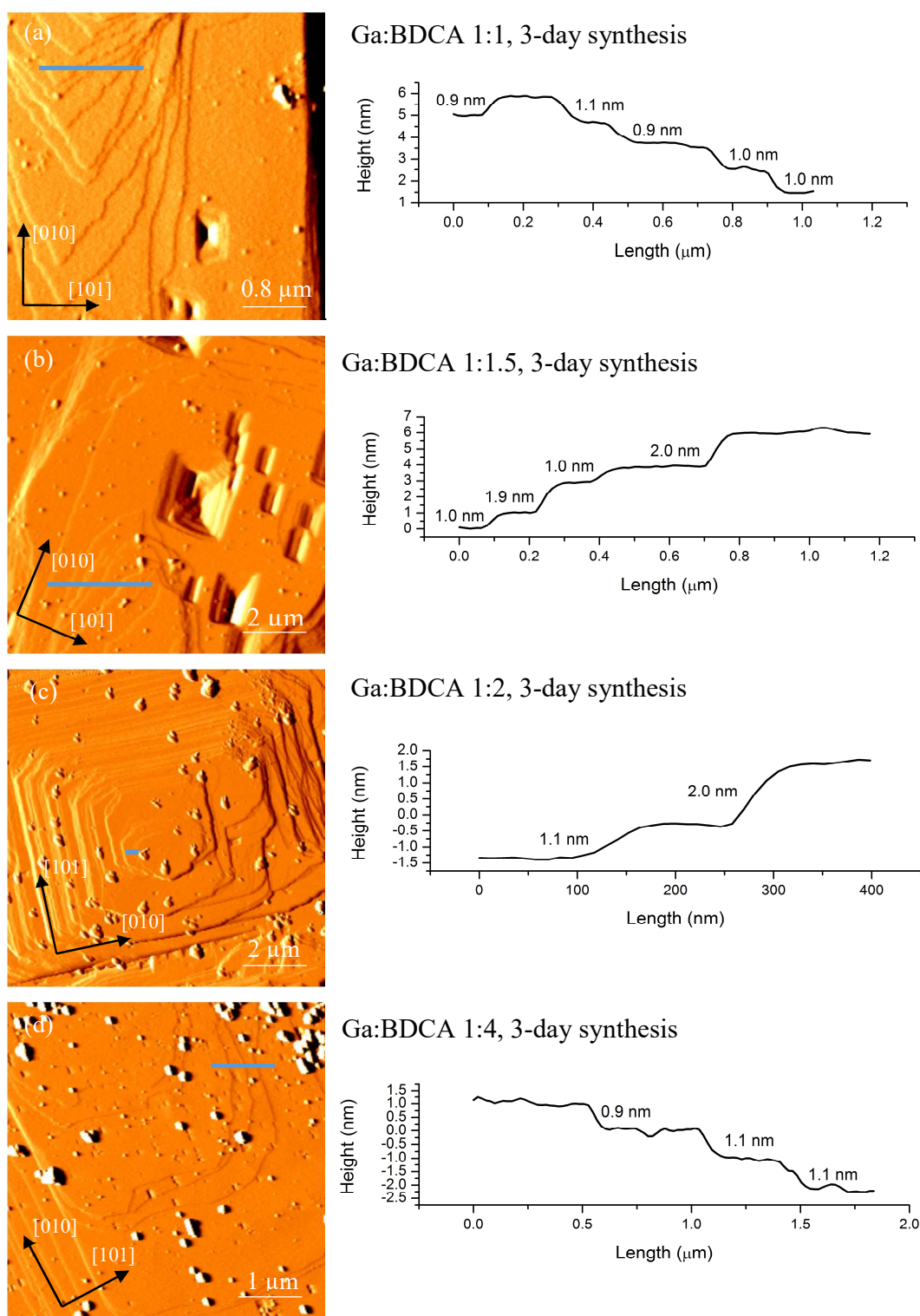


Figure 3-12 AFM error images from 1:1, 1:1.5, 1:2, and 1:4 syntheses. All syntheses were conducted for a duration of 3 days.

During the 1:2 experiments with a shorter synthesis time, growth hillocks could develop into similar hexagonal shape. The morphology observed in those experiments is possibly due to the shorter crystallization time, and it is assumed to evolve into rectangular shape if enough time is given (Figure 3-9). However, for our 1:1 experiments, most hexagonal hillocks failed to develop rectilinear terraces along the [101] direction, even though they were allowed to grow for 3 days (Figure 3-12a). Few more experiments with a ratio range from 1:1 to 1:2 were performed, and their AFM results are shown in Figure 3-12. In some of those experiments, growth hillocks have co-existing hexagonal and rectangular layers. On the other hand, when a 1:4 ratio was employed, most terraces observed are rectangular similar to the 1:2 experiments. It appears that given the same synthesis time, hillocks with a smaller Ga:BDCA ratio are more likely to convert from hexagonal to rectangular as they grow.

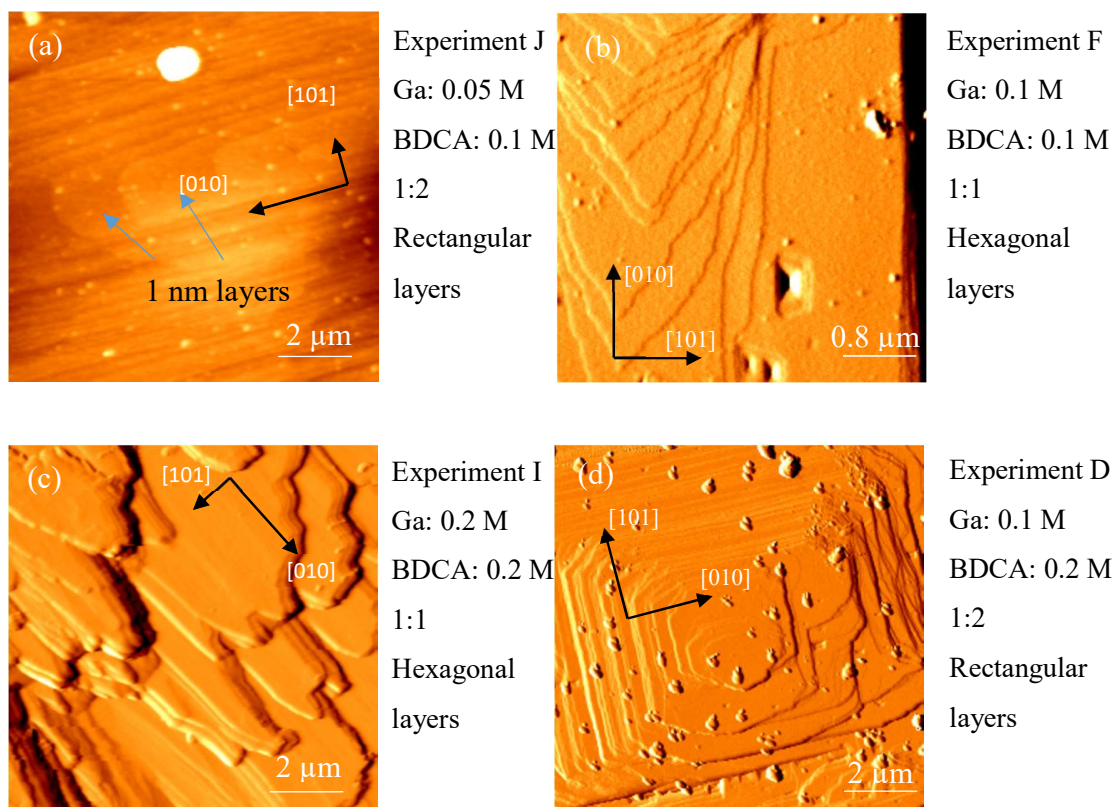


Figure 3-13 Comparison of layer morphologies from 1:1 and 1:2 synthesis experiments with same BDCA starting concentration. (a) is a topography image and (b-d) are error images.

Another factor that is different between the 1:1 and 1:2 experiments is that the 1:1 experiments have a lower concentration of BDCA than the 1:2 experiments. To further prove that the variation in terrace morphology is due to the changed Ga:BDCA ratio rather than decreased BDCA supersaturation, experiments I and J were performed (Figure 3-13). Experiment J is also a 1:2 synthesis, but the volume of water used was doubled from 10 mL to 20 mL. Thus the starting amount of BDCA would be equal to that in experiment F, which is a 1:1 synthesis. From Figure 3-13a, it can be seen that although the corners are more rounded, terraces obviously adopted the shape of rectangle. Monolayers in this sample show no difference than those in previous samples, which have the height around

1.0 nm. Following the same idea, another 1:1 experiment I was performed, where the amount of gallium nitrate and BDCA used were doubled to achieve the same BDCA starting concentration used in Experiment D, which is a regular 1:2 synthesis. The results are shown in Figure 3-13c. Most layers measured are macro-steps with heights ranging from tens to hundreds of nanometers. It is possibly owing to the rapid nucleation on the surface caused by the higher degree of supersaturation. Similar hexagonal growth pattern is clearly followed in the formation of those macro-steps.

In Section 3.3.2, it has been discussed that the advancement rate of the hexagonal side edges (r_c) gradually becomes greater than $r_{[010]}$, which explains the formation of rectangular-shaped terraces after 3 days' crystallization. Thus it can be concluded that Ga:BDCA ratio clearly has an effect on the relationship between r_c and $r_{[010]}$ in the crystal growth process.

3.3.4 Investigations on Surface Changes of Ga-MIL-53 Induced by “Breathing Effect”

The MIL-53 MOF is known to exhibit the “breathing effect”.³ Analogues of this MOF have a flexible network that can alter its pore dimensions and crystal phase to accommodate different species of guest molecules. In addition, changes in the surfaces of MIL-53 crystallites after phase transitions induced by the “breathing effect” were examined.

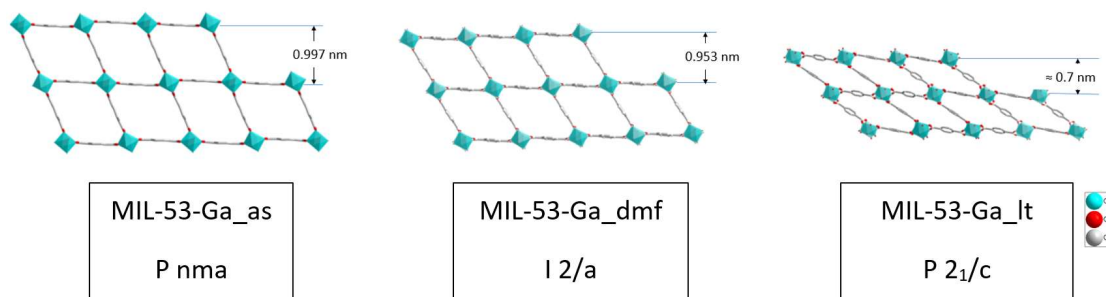


Figure 3-14 The MIL-53(Ga) structure for three phases. Hydrogen atoms are omitted for clarity.

Previous surface examinations were conducted on the as made samples, where the size of the channels were shaped by the excess BDCA molecules inside. When they are added to DMF and heated to 200°C for 10 hours, the trapped BDCA will be exchanged by DMF. During the process, phase transition is induced by the different interaction that BDCA and DMF have with the framework. The channels are evacuated at 200°C under vacuum, and readily adsorbs water inside when exposed to air. The framework will shrink due to the hydrogen bond between water and carboxylate group in the ligand, transforming to the form of Ga-MIL-53_lt.

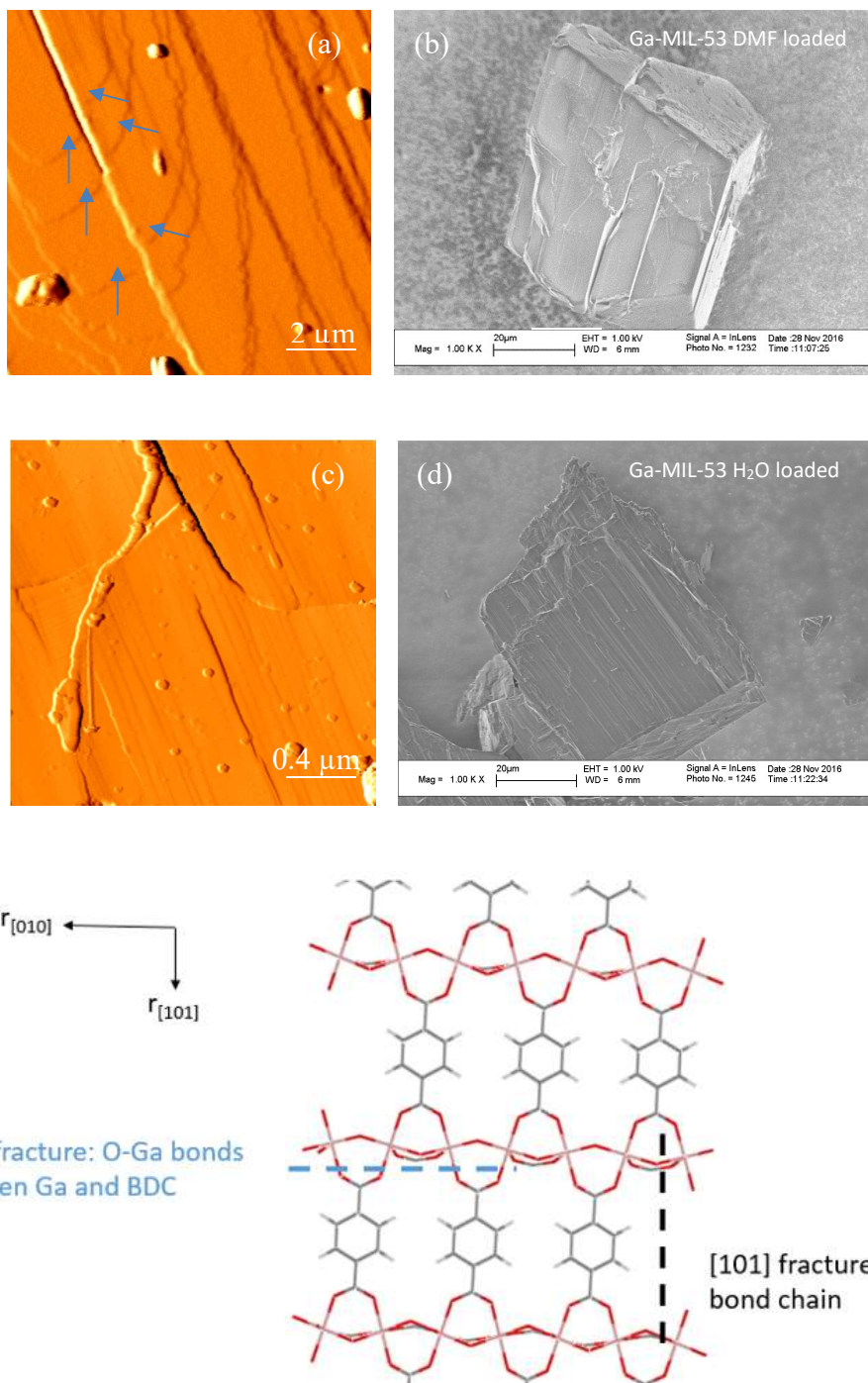


Figure 3-15 AFM error images and SEM micrographs on Ga-MIL-53_dmf (a-b) and Ga-MIL-53_It (c-d). (e) is a schematic representation of a single {101} layer.

Figure 3-15 shows that after the framework breathes, traces of previous growth features can still be found on Ga-MIL-53_dmf and Ga-MIL-53_lt, and they can be used as reference when the changes on the surface are investigated. One notable difference is the frequent fracturing observed on the surface. In the formation of a fracture, it is most likely that the strong intramolecular covalent bonds of the BDC ligand are not broken. Thus most likely it is Ga-BDC bond or Ga-O bond that breaks when a fracture occurs. It can also be seen that fractures along [101] are less frequent than fractures along [010]. This could either be due to the stronger bond strength of the Ga-O bond than Ga-BDC bond, thus the inorganic Ga-O-Ga bond chain is harder to break (Figure 3-15e); or possibly it can be explained by the anisotropy of the internal stress in the lattice induced by phase transition, as studies have suggested that the breathing behavior is achieved by adjusting the size of the rhombus channel, leaving the inorganic bond chain unchanged.²⁰ In Figure 3-15a, it can also be observed that step patterns have moved across the fracture, as indicated by the blue arrows. This suggests that planes may also slip along fracture when phase transition occurs. Similar surfaces could also be observed on MIL-53_lt samples (Figure 3-15c, 15d).

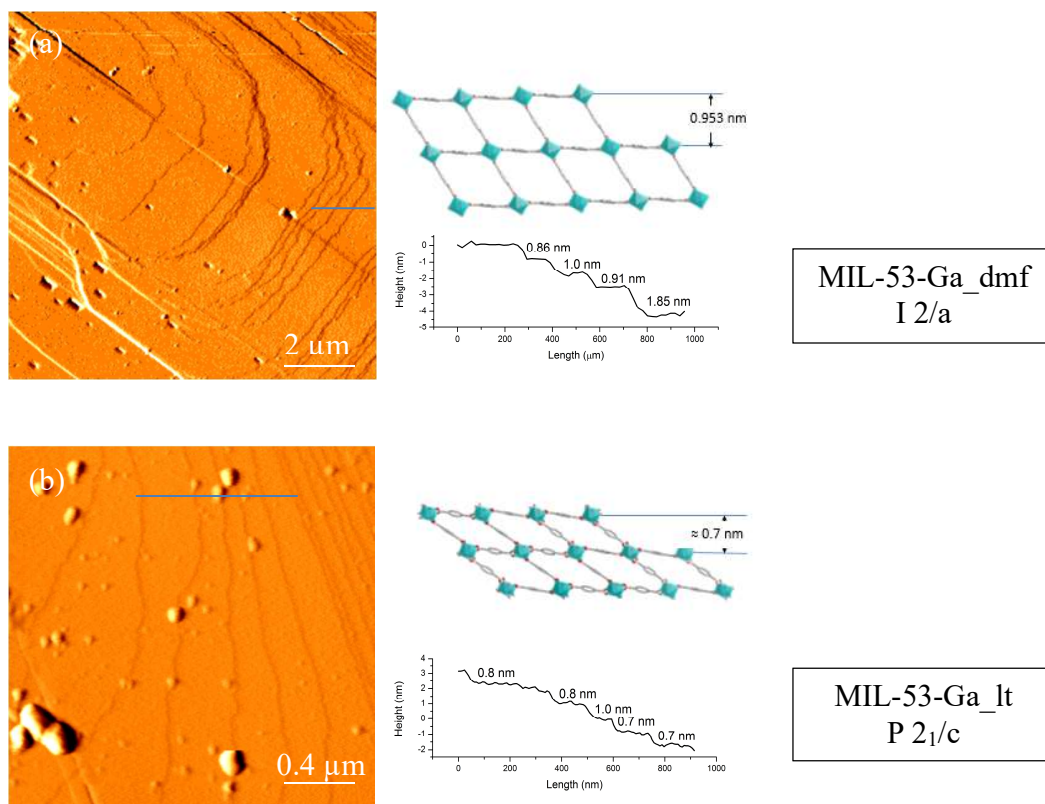


Figure 3-16 (a) AFM error image captured on Ga-MIL-53_dmf. (b) AFM error image captured on Ga-MIL-53_lt. Height profiles along the blue lines are shown on the right of corresponding images.

The crystallographic spacing of the rhombus cell also changes as the framework adapts into different phases. They are 0.99 nm for Ga-MIL-53_as, and 0.95 nm for Ga-MIL-53_dmf, respectively. For the Ga-MIL-53_lt, there exists three chemically different Ga sites,⁶ thus distances between Ga octahedra in adjacent layers will vary to a small extent and float around 0.7 nm when different Ga sites were chosen. When the framework “breathes”, it is also expected that the height of the layer will change as well. The layer heights of 0.86 nm and 1.8 nm observed in Figure 3-16a can be explained by the decrease of spacing from 0.99 nm to 0.95 nm when the framework transforms from Ga-MIL-53_as to Ga-MIL-53_dmf, as the heights of layers measured in the as-made samples are rarely

below 0.9 nm. The change of layer height becomes more evident when the surface of It phase is examined. However, it can be seen that some layers are observed to have heights of 0.8 nm and 1.0 nm, which is different from the theoretical spacing of 0.7 nm (Figure 3-16b).

During the phase transitions of Ga-MIL-53, majority of the diamond-shaped channels should transform into similar dimensions, as indicated by the long-range ordering obtained from X-ray diffraction data. However, AFM results show that on the surface, some of the diamond-shaped channels may be more compressed or expanded than others in the framework. Internal stress within the lattice is possibly one of the reasons that stops those observed surface layers from changing into their expected heights.

3.4 Conclusion

To conclude, single crystals of Ga-MIL-53 with a flexible framework have been successfully prepared via hydrothermal method under different conditions. AFM, SEM and XRD were used to characterize the material. The surfaces of $\{101\}$ were found to grow through both the “birth and spread” and “spiral” crystal growth mechanisms, with rectangular shaped growth hillocks evident due to anisotropic growth. The anisotropy of growth on the surface is dependent on both reaction time and Ga/BDCA ratio used during the synthesis. The findings suggest that crystal growth on the $\{101\}$ faces undergoes more than one stage where growth rates along different crystallographic directions change to give different terrace morphologies. By exploring possible surface termination structures, the fundamental growth units during the self-assembly process are discussed.

The work in this chapter also reveals the changes in the surfaces of Ga-MIL-53 crystallites after phase transitions induced by the “breathing effect”. In particular, AFM experiments have allowed the observation of cell compression on the surface, and AFM/SEM experiments combined have provided detailed information regarding frequent fracturing after phase changes.

3.5 References

1. Vougo-Zanda, M.; Huang, J.; Anokhina, E.; Wang, X.; Jacobson, A. J., Tossing and turning: Guests in the Flexible Frameworks of Metal (III) Dicarboxylates. *Inorganic Chemistry* **2008**, *47* (24), 11535-11542.
2. Zhang, Y.; Lucier, B. E.; Huang, Y., Deducing CO₂ Motion, Adsorption Locations and Binding Strengths in a Flexible Metal-Organic Framework without Open Metal Sites. *Physical Chemistry Chemical Physics* **2016**, *18* (12), 8327-8341.
3. Serre, C.; Millange, F.; Thouvenot, C.; Noguès, M.; Marsolier, G.; Louër, D.; Férey, G., Very Large Breathing Effect in the First Nanoporous Chromium (III)-Based Solids: MIL-53 or Cr^{III} (OH)· {O₂C-C₆H₄-CO₂}· {HO₂C-C₆H₄-CO₂H}_x·H₂O_y. *Journal of the American Chemical Society* **2002**, *124* (45), 13519-13526.
4. Serra-Crespo, P.; Dikhtiarenko, A.; Stavitski, E.; Juan-Alcañiz, J.; Kapteijn, F.; Coudert, F.-X.; Gascon, J., Experimental Evidence of Negative Linear Compressibility in the MIL-53 Metal-Organic Framework Family. *CrystEngComm* **2015**, *17* (2), 276-280.
5. Biswas, S.; Ahnfeldt, T.; Stock, N., New Functionalized Flexible Al-MIL-53-X (X=-Cl,-Br,-CH₃,-NO₂,-(OH)₂) Solids: Syntheses, Characterization, Sorption, and Breathing Behavior. *Inorganic Chemistry* **2011**, *50* (19), 9518-9526.

6. Volkringer, C.; Loiseau, T.; Guillou, N.; Férey, G.; Elkaïm, E.; Vimont, A., XRD and IR Structural Investigations of a Particular Breathing Effect in the MOF-type Gallium Terephthalate MIL-53 (Ga). *Dalton Transactions* **2009**, (12), 2241-2249.
7. Bishop, A. C., *An Outline of Crystal Morphology*; Hutchinson Scientific and Technical: London, 1967.
8. Harker, D., A New Law of Crystal Morphology, Extending the Law of Bravais. *Amer. Mineral* **1937**, 22, 446-467.
9. Widlak, N.; Hartel, R. W.; Narine, S., *Crystallization and Solidification Properties of Lipids*. The American Oil Chemists Society: 2001.
10. Moh, P. Y.; Cubillas, P.; Anderson, M. W.; Attfield, M. P., Revelation of the Molecular Assembly of the Nanoporous Metal Organic Framework ZIF-8. *Journal of the American Chemical Society* **2011**, 133 (34), 13304-13307.
11. Wagia, R.; Strashnov, I.; Anderson, M. W.; Attfield, M. P., Determination of the Preassembled Nucleating Units That Are Critical for the Crystal Growth of the Metal–Organic Framework CdIF-4. *Angewandte Chemie International Edition* **2016**, 55 (31), 9075-9079.
12. Smith, R. L.; Lind, A.; Akporiaye, D.; Attfield, M. P.; Anderson, M. W., Anatomy of Screw Dislocations in Nanoporous SAPO-18 as Revealed by Atomic Force Microscopy. *Chemical Communications* **2015**, 51 (28), 6218-6221.
13. Sunagawa, I., *Crystals: Growth, Morphology, and Perfection*. Cambridge University Press: Cambridge, 2005.
14. Cubillas, P.; Anderson, M. W.; Attfield, M. P., Crystal Growth Mechanisms and Morphological Control of the Prototypical Metal-Organic Framework MOF-5

- Revealed by Atomic Force Microscopy. *Chemistry-A European Journal* **2012**, *18* (48), 15406-15415.
15. Cubillas, P.; Anderson, M. W.; Attfield, M. P., Influence of Isomorphous Substituting Cobalt Ions on the Crystal Growth of the MOF-5 Framework Determined by Atomic Force Microscopy of Growing Core-Shell Crystals. *Crystal Growth & Design* **2013**, *13* (10), 4526-4532.
 16. Nie, H.-Y.; McIntyre, N., A Simple and Effective Method of Evaluating Atomic Force Microscopy Tip Performance. *Langmuir* **2001**, *17* (2), 432-436.
 17. Mullin, J. W., *Crystallization*. Butterworth-Heinemann: Oxford, **2001**.
 18. Sours, R. E.; Zellelow, A. Z.; Swift, J. A., An in-situ Atomic Force Microscopy Study of Uric Acid Crystal Growth. *The Journal of Physical Chemistry B* **2005**, *109* (20), 9989-9995.
 19. Moh, P. Y.; Brenda, M.; Anderson, M. W.; Attfield, M. P., Crystallisation of Solvothermally Synthesised ZIF-8 Investigated at the Bulk, Single Crystal and Surface Level. *CrystEngComm* **2013**, *15* (45), 9672-9678.
 20. Seoane, B.; Sorribas, S.; Mayoral, Á.; Téllez, C.; Coronas, J., Real-time Monitoring of Breathing of MIL-53 (Al) by Environmental SEM. *Microporous and Mesoporous Materials* **2015**, *203*, 17-23.

Chapter 4

4 Investigating Crystal Growth of M-SDB Metal-Organic Frameworks

4.1 Introduction

The absorption and storage of CO₂ have always been an important motivation for the new development of porous materials. Recently, a series of MOF that uses 4, 4'-sufonyldibenzoate (SDB) as organic ligand has attracted much attention due to their high CO₂ affinity and selectivity.¹⁻³ Different from other CO₂ absorbing MOFs that have open-metal sites or polar functional groups, the M-SDB (M=Ca, Pb, Cd) MOFs have the capacity to selectively absorb CO₂ under relatively high humidity. Such preferred absorption of CO₂ is found to originate from SDB ligand's unique geometry when incorporated into the framework. As Figure 4-1 shows, the SDB ligand has unique V- shaped pocket and CO₂ could interact with both phenol rings by being positioned equally between the rings.⁴⁻⁵ Among different surface techniques, AFM has proven to be a powerful tool to understand self-assembly process and surface features of MOFs⁶⁻¹¹. In this chapter, AFM studies will be conducted on the Pb, Ca and Cd analogues of SDB series due to their interesting properties.

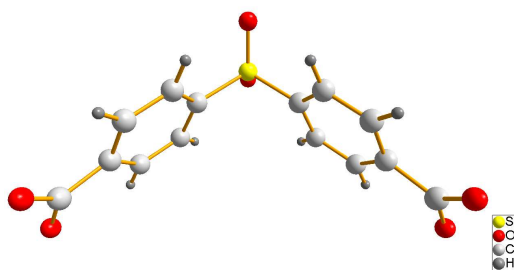


Figure 4-1 Structure of the V-shaped SDB ligand.

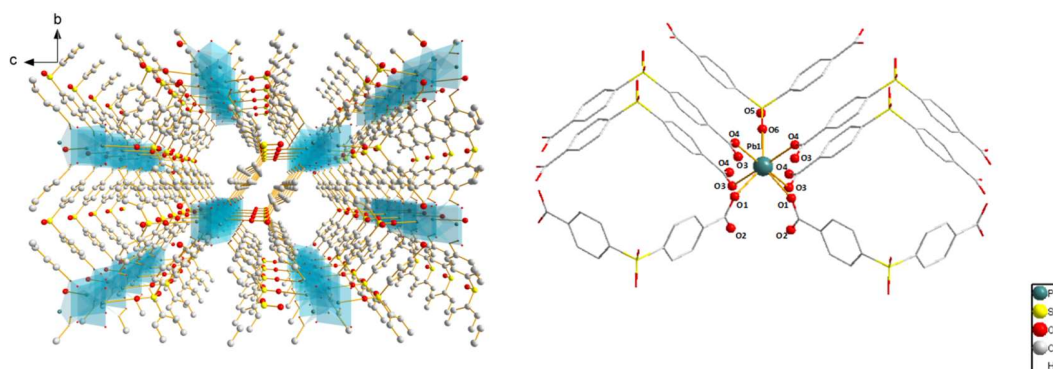


Figure 4-2 (Left) structure of PbSDB viewed along a axis; (Right) Local structure and Lead coordination environment of PbSDB.

As the first reported SDB MOF, PbSDB has been broadly studied and is found to process high CO_2/N_2 selectivity.^{1, 4} In the framework the lead ion is bonded to seven oxygens where six come from different SDB^{2-} anions and the other one is from the sulfonyl group. The resulting network has a straight 1D channel along the a axis. This compound has an orthorhombic space group Pnma.

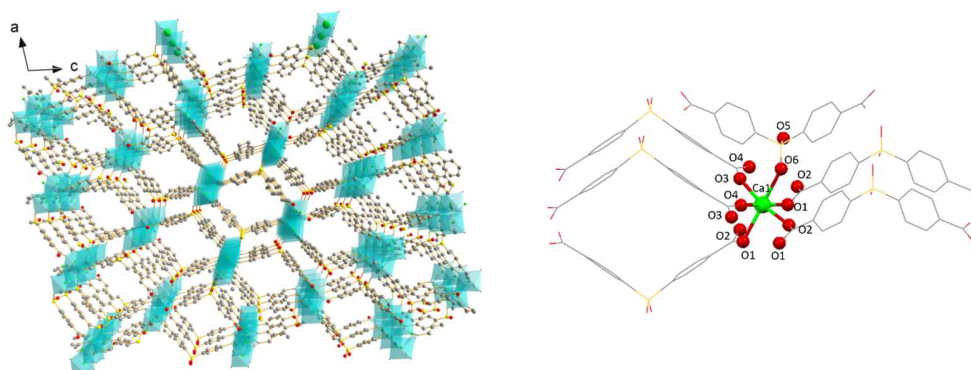


Figure 4-3 (Left) structure of CaSDB viewed along b axis; (Right) Local structure and Calcium coordination environment of CaSDB.

The non-toxic calcium ion could also coordinate with SDB ligands to form a 3D framework, with a straight channel along its b axis.² Other than the strong affinity to CO₂ shared with other SDB MOFs, CaSDB also shows great potential for Xe/Kr separation based on its unique selectivity for the former over the latter.¹² The CaSDB network has a different connectivity where each Ca ion is only bonded to five carboxylate oxygens and one sulfonyl oxygen. As a result, the compound is crystalized in a P2₁/n monoclinic framework.

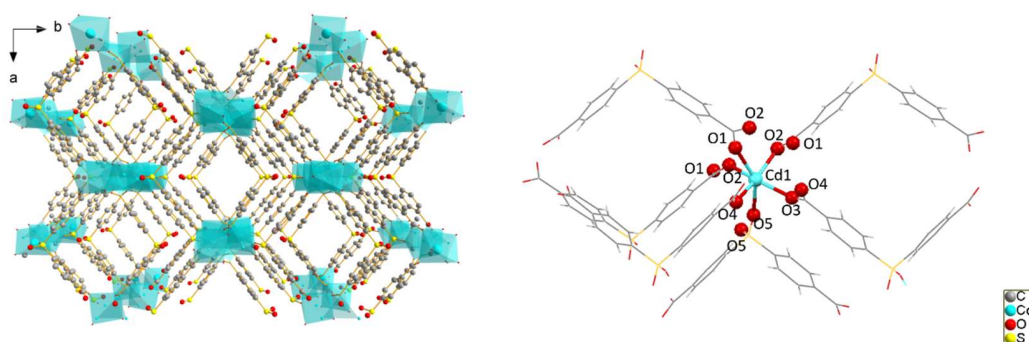


Figure 4-4 (Left) structure of CdSDB viewed along c axis; (Right) Local structure and Cadmium coordination environment of CdSDB.

CdSDB is the last SDB-based MOF studied in this chapter with the motivation of better understanding the influence of various metal centers has in crystal growth.^{3, 13} CdSDB crystallizes in an entirely different P2/c space group, and Cd ions are six-coordinated to five carboxylate oxygens and one sulfonyl oxygen. Despite the same coordination number with Ca ions in CaSDB, the Cd ions are not perfectly aligned along the 1D channel. As a result, the channel is “sinusoidal” and different than the straight channel seen in CaSDB. In summary, Pb, Ca and Cd can be joined by SDB ligand to form three different

frameworks, hence it is worth investigating if the analogs share any similar surface features.

4.2 Experimental

4.2.1 Sample Preparation

All samples were prepared according to references with slight modifications¹⁻³ and all reagents and solvents used were purchased from Sigma-Aldrich.

For the hydrothermal synthesis of PbSDB, 0.5 mmol of $\text{Pb}(\text{NO}_3)_2$ were mixed with 1 mmol 4,4'-sulfonyldibenzoic acid by 10 ml of a 1:1 mixed solvent of DMF and methanol. The mixture was then heated at 160 °C for 1 day. The product was colorless needle-shaped crystals and was collected via filtration.

CaSDB was prepared under hydrothermal conditions from $\text{Ca}(\text{NO}_3)_2$ and sulfonyldibenzoic acid mixed in 3 mL ethanol and 7 mL of water. Two experiments with different starting amounts of metal salt/ligand were conducted, and the usages were summarized in the Table 4-1. During the synthesis, the temperature was elevated to 180°C for 3 days.

Table 4-1 Summary of synthesis conditions of CaSDB

Experiment	Calcium Nitrate (M)	SDBA (M)	Molar ratio
A	0.06	0.03	1:0.5
B	0.06	0.06	1:1

CdSDB was also prepared using hydrothermal method. 1 mmol of $\text{Cd}(\text{NO}_3)_2$ and 1 mmol 4,4'-sulfonyldibenzoic acid were mixed in a 10 mL solvent, which composes of 7 mL ethanol and 3 mL water. The mixture was heated at 180 °C for 3 days. Colorless needle-shaped crystals were recovered *via* filtration.

4.2.2 Characterization

AFM measurements. AFM observations were made using a Park Systems XE-100 Atomic Force Microscope. Square aluminum plates were used to place the single crystals. To eliminate the movement of sample crystals during the scan when they physically contact with the AFM tip, adhesive tapes were attached to the surface of the plates before sample application. All the measurements were conducted under the dynamic force mode in air at room temperature. A cantilever with a nominal spring constant of 40 N/m, the resonant frequency of 300 kHz is used, and the tip has a radius of 10 nm. The scan rate varies from 0.5 Hz to 1 Hz depending on the scale of the image; generally slower scan rate is used for larger images to obtain optimum image quality. The XEI image process software package was used to perform image flattening and height analysis.

X-ray Diffraction. An Inel CPS Powder Diffractometer with a $\text{Cu K}\alpha$ radiation ($\lambda = 1.5406 \text{ \AA}$) was used to acquire pXRD patterns for routine characterization in the 2θ range of 5-120°.

Habit prediction. Relative surface areas for dominant crystallographic planes were calculated using the built in BFDH calculation function of the Mercury software.

SEM. All scanning electron micrographs were captured using an LEO (Zeiss) 1540XB FIB/SEM instrument.

4.3 Results and Discussion

4.3.1 PbSDB

In this section, AFM is used to examine one of the SDB-based MOF, PbSDB. The MOF is synthesized under hydrothermal conditions. Figure 4-5 shows the scanning electron micrographs of PbSDB single crystals. The single crystals adopt a needle-shaped habit. The size of the single crystals varies, with large ones exceeding 500 μm in length and 30 μm in width. The preliminary assessment is that the crystal is bounded by $\{011\}$ elongated faces based on its orthorhombic crystal system.¹⁴

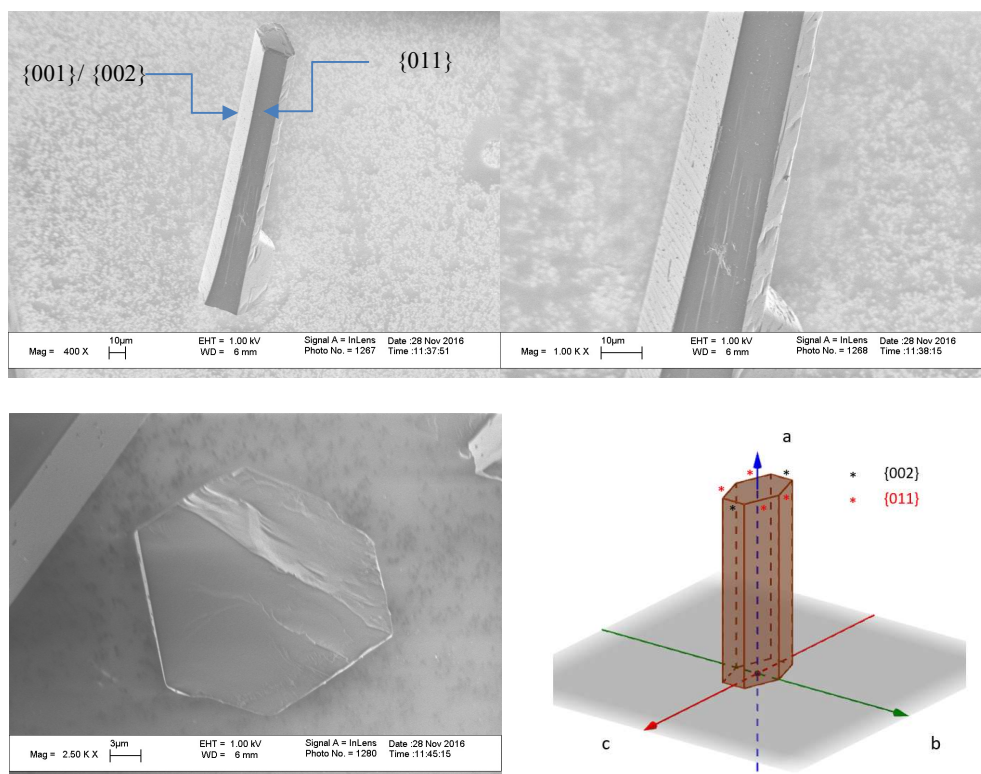


Figure 4-5 Scanning electron micrographs of PbSDB single crystals revealing $\{001\}$ and $\{011\}$ facets.

BFDH habit calculation shows that $\{011\}$ facets cover 57.7% of the total area. The simulation also suggests the existence of $\{002\}$ facets, making up 18.62% of the total facet area. This result is consistent with the SEM micrographs which reveal the presence of six faces on the side. From the considerations of symmetrical relations, four of them are identified as $\{011\}$ and the rest two are labeled as $\{002\}$.

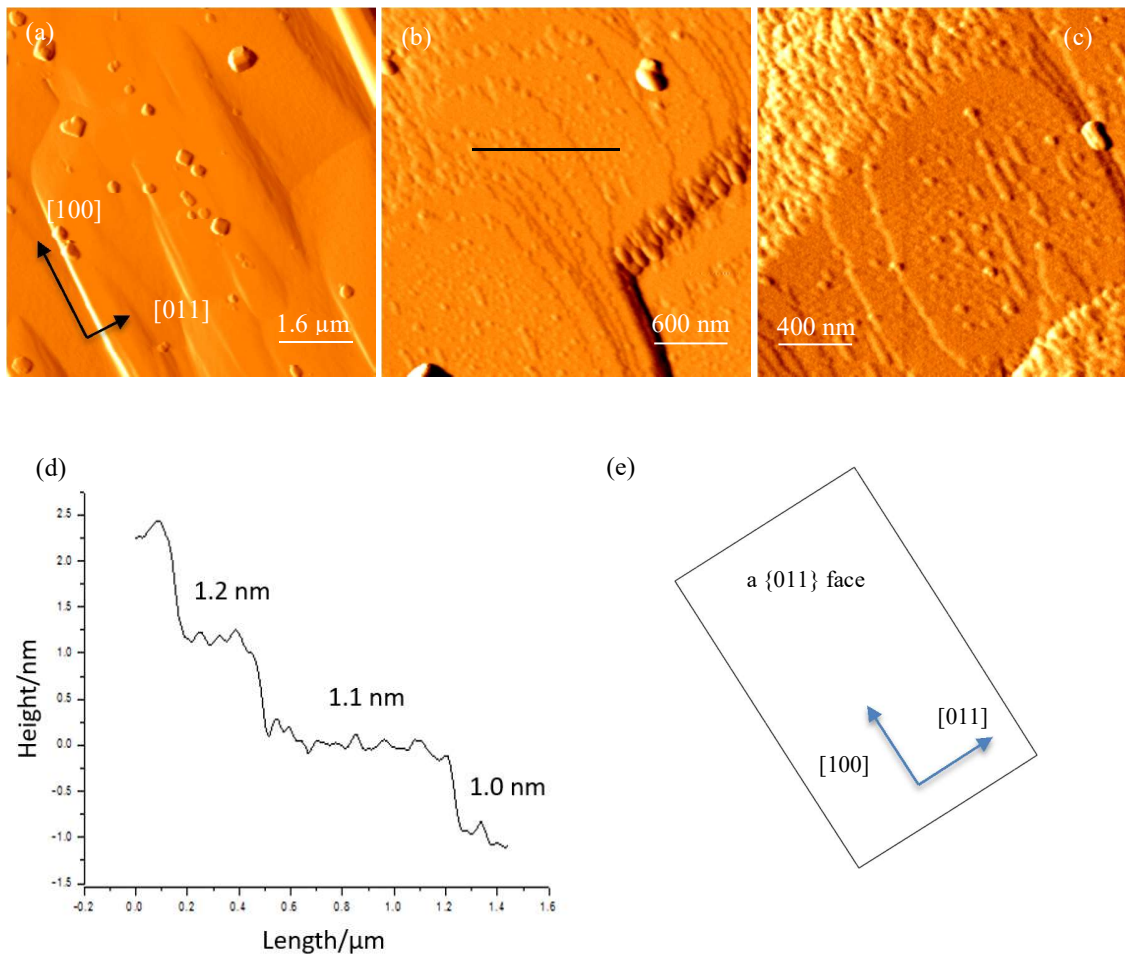


Figure 4-6 (a) is an overview of a $\{011\}$ face and (b) and (c) are the zoom in images showing rectangular growth hillocks and elongated nuclei. (d) shows the height profile measured along the blue line in (b). (e) describes the orientation of the $\{011\}$ face scanned.

Figure 4-6 shows the error images taken on the large rectangular faces. On the $\{011\}$ faces elongated layered growth hillocks and nuclei were observed, showing a “birth and spread” growth mechanism.¹⁵ The terrace morphology is rectangular in shape. The rectilinear nature of the terraces is due to the anisotropic growth, with growth along the $[100]$ direction more favorable than the growth along the $[011]$ direction. Thus the particles with square and rhombus shape in Figure 4-6a are more likely to be smaller separate single crystals adhered to the surface rather than newly developed nuclei. Figure 4-6b and 4-6c are zoomed in images on one of the layered hill. Interestingly, it can be seen that the edges parallel to the $[011]$ direction are “fuzzy” while the edges parallel to $[100]$ direction are relatively smooth. The relative smoothness of the edges can be interpreted in terms of kink density. The kink density along a smooth step edge is small and vice versa. Such a difference in edge smoothness could be related to the anisotropic bond strengths along the two directions.¹⁶ According to the Kossel model, growth units are more readily incorporated onto kinked sites. It is consistent with the observation that growth along the $[100]$ is more rapid than that along $[011]$.

Cross-sectional analysis indicates that most of the monolayers and nuclei develop into three heights within the error of 0.1 nm. The heights are 1.0, 1.1 and 1.2 nm. Consecutive observations are made from different regions of the surface and no preferences of one height over the others are found. The steps and nuclei with all three heights are distributed randomly. This strongly suggests that more than one stable termination structure are present on the $\{101\}$ surface.

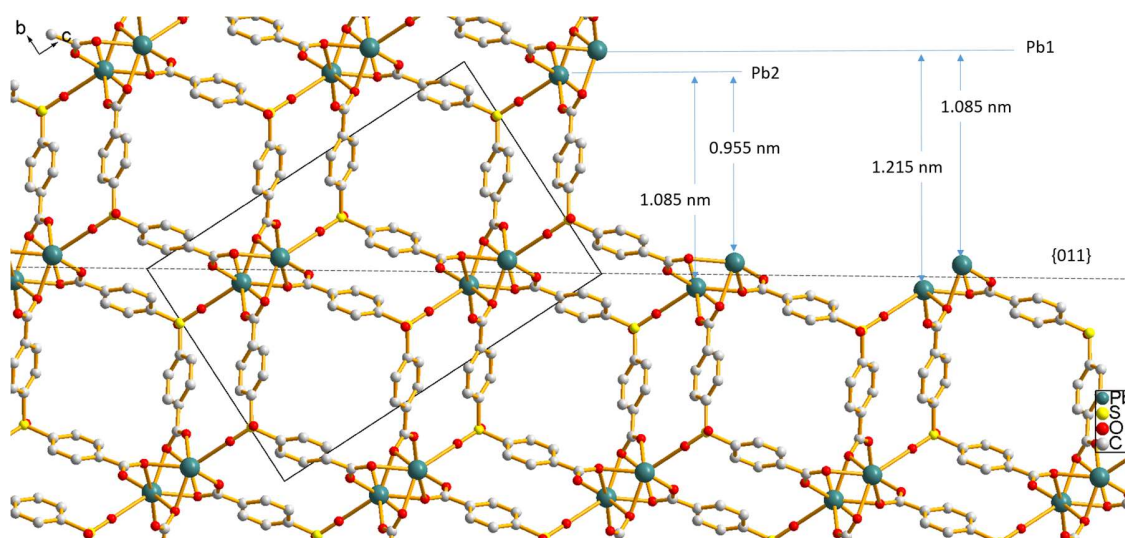


Figure 4-7 PbSDB framework structure viewing through [100] direction.

More information about the formation of the steps can be retrieved by relating the measured heights with the plausible layer spacings within the crystal structure. Growth normal to the $\{011\}$ plane involves two Pb ions linked by the SDB ligand. For demonstration purposes, the top Pb ion along the $[011]$ direction is labeled as Pb1 and the lower Pb ion is labeled Pb2, despite the fact that they are chemically and crystallographically equivalent. The layer height of 1.1 nm corresponds to the d_{011} spacing of 1.085 nm. This height matches well with the height difference either between two closest Pb1 ions or between two nearest Pb2 ions. The layer of 1.20 nm height can be explained by the termination at the upper Pb1 and the lower Pb2 ions. With the same idea, the height of 1.0 nm could be caused by the addition of one SDB ligand and Pb2 ion upon a Pb1 ion which has a theoretical spacing of 0.95 nm, as illustrated in Figure 4-7.

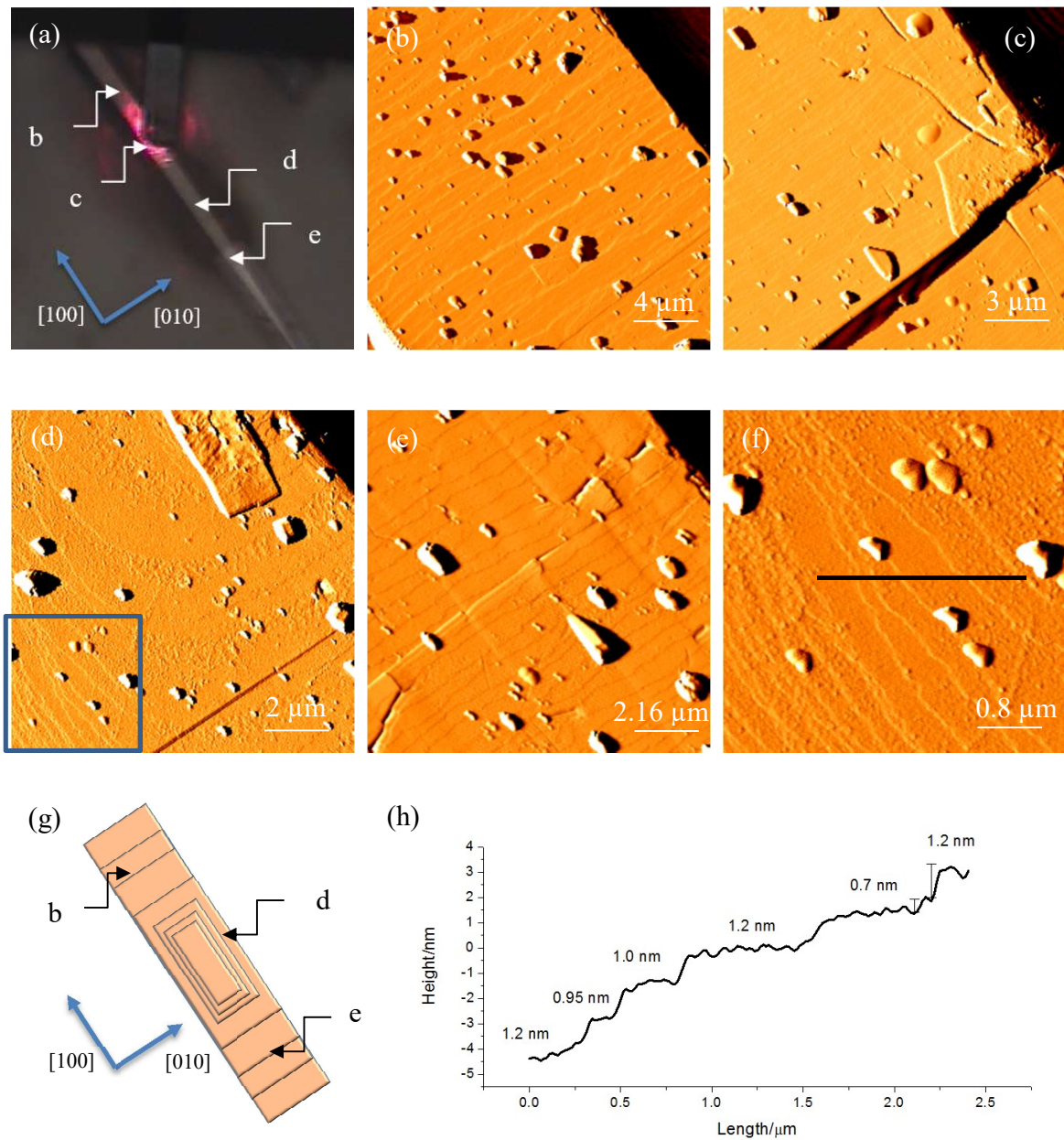


Figure 4-8 (a) shows the optical microscopic image with a {002} face on top. (b), (c), (d), (e) and (f) are AFM deflection image captured from different regions of the {002} face in (a). The zoomed in image of the blue box in (d) is shown in (f). (g) is a scheme showing layer pattern on the surface. (h) shows cross-section analyses taken along the black line in (f).

Figure 4-8 shows the optical and AFM images of a PbSDB single crystal featuring a {002} face. It can be seen that the {002} face gradually narrows, eventually vanishes at the end.

This is possibly due to its faster growth rate than the two neighboring $\{011\}$ faces. AFM observations are made in different regions of the surface as labeled in Figure 4-8a. In the middle of the face (Figure 4-8d), the growth hillock can be observed to also follow the “birth and spread” mechanism. The steps parallel to the $[100]$ direction are only visible in this region. The step edge parallel to the $[100]$ direction later vanishes as they hit the edge of the surface. Unlike $\{011\}$ planes, coalescence of multiple growth hillocks is not common, and the steps on this surface appear as they all originate from the spreading of the growth hillock shown in Figure 4-8d. This suggests that this region might be firstly formed during crystallization.

Measurements across the steps yield a height of 1.0 ± 0.1 nm. This height corresponds to the d_{002} spacing. Heights of 0.7 and 1.2 ± 0.1 nm are also revealed, which are in good agreement with the theoretical spacings shown in Figure 4-9. It can be deduced that the three different heights are due to the presence of two different positioned Pb ions, which is consistent with the discussion on $\{101\}$ surfaces in the previous section.

In summary, “birth and spread” is still the growth mechanism on $\{002\}$ planes, and height measurements on the basic steps have confirmed three different surface structures, which is in good agreement with our findings from $\{011\}$ planes.

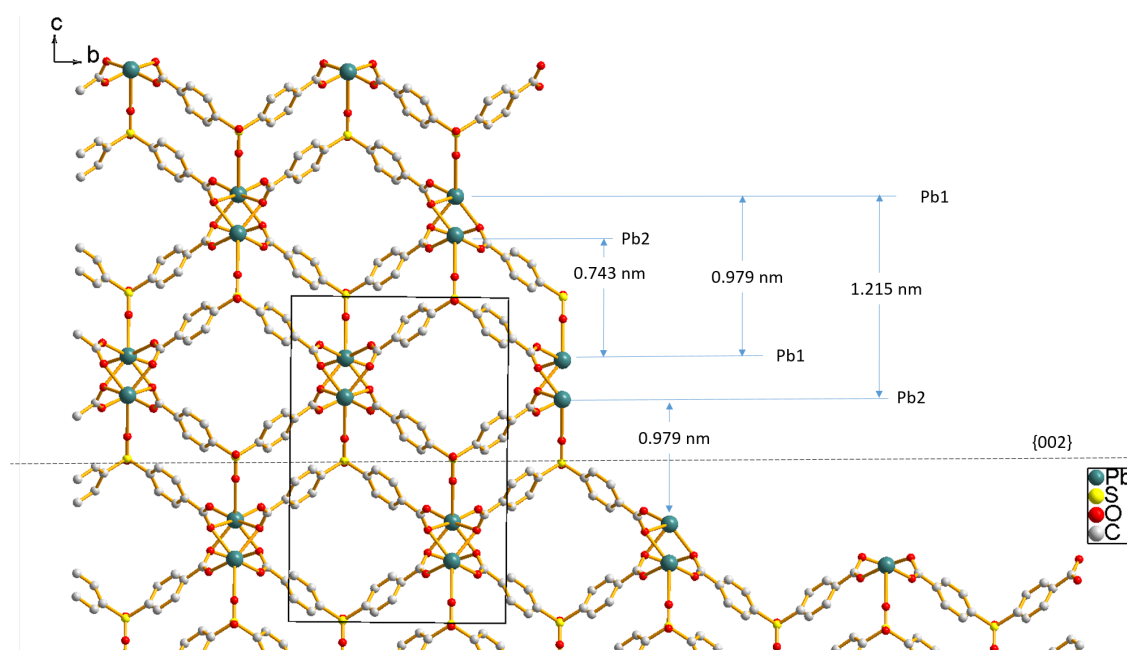


Figure 4-9 PbSDB framework structure viewing through [100] direction. The black box represents the unit cell.

4.3.2 CaSDB

As the calcium analog of SDB series MOF, CaSDB's non-toxic nature of its metal center makes it more attractive for applications than its Pb counterpart. Different from Pb's seven coordination in PbSDB, the calcium ions are only bonded to six oxygens. With a similar, but not identical structure, CaSDB has been chosen to be the subject of AFM studies in this section.

Figure 4-10 shows the single crystals of CaSDB captured under an optical microscope. It can be seen that they adopt a bladed or plate form, and the lengths vary from 50 μm to exceeding 1000 μm . BFDH calculation shows that $\{\bar{1}01\}$, $\{002\}$ and $\{101\}$ are the three most dominant sets of planes to appear in the crystal habit, with $\{\bar{1}01\}$ planes predicted to cover 31% of the total area, $\{002\}$ to cover 29% of the total area and $\{101\}$ to cover 17%

of the total area. Note that due to its monoclinic crystal system, $\{\bar{1}01\}$ and $\{101\}$ are not equivalent sets of planes. From the optical images, however, only four faces can be identified. The face index will be discussed later by comparing the heights observed from cross-sectional profiles of single layers with crystallographic spacings.

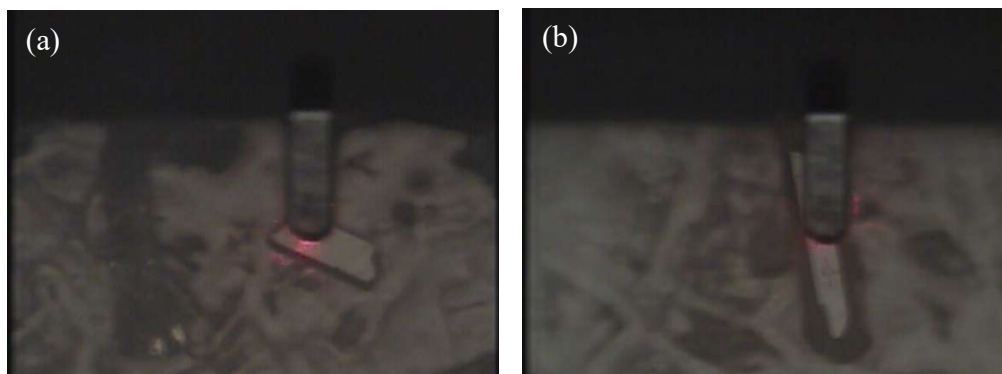


Figure 4-10 Two different crystals of CaSDB from synthesis A under optical microscope.

Multiple successful attempts were made to synthesize CaSDB single crystals, with reaction conditions summarized in Table 4-1. The stoichiometry used in experiment B comes from literature sources,² and experiment A was conducted by varying the amount of SDB ligands used. The solvent, temperature and reaction time were kept unchanged.

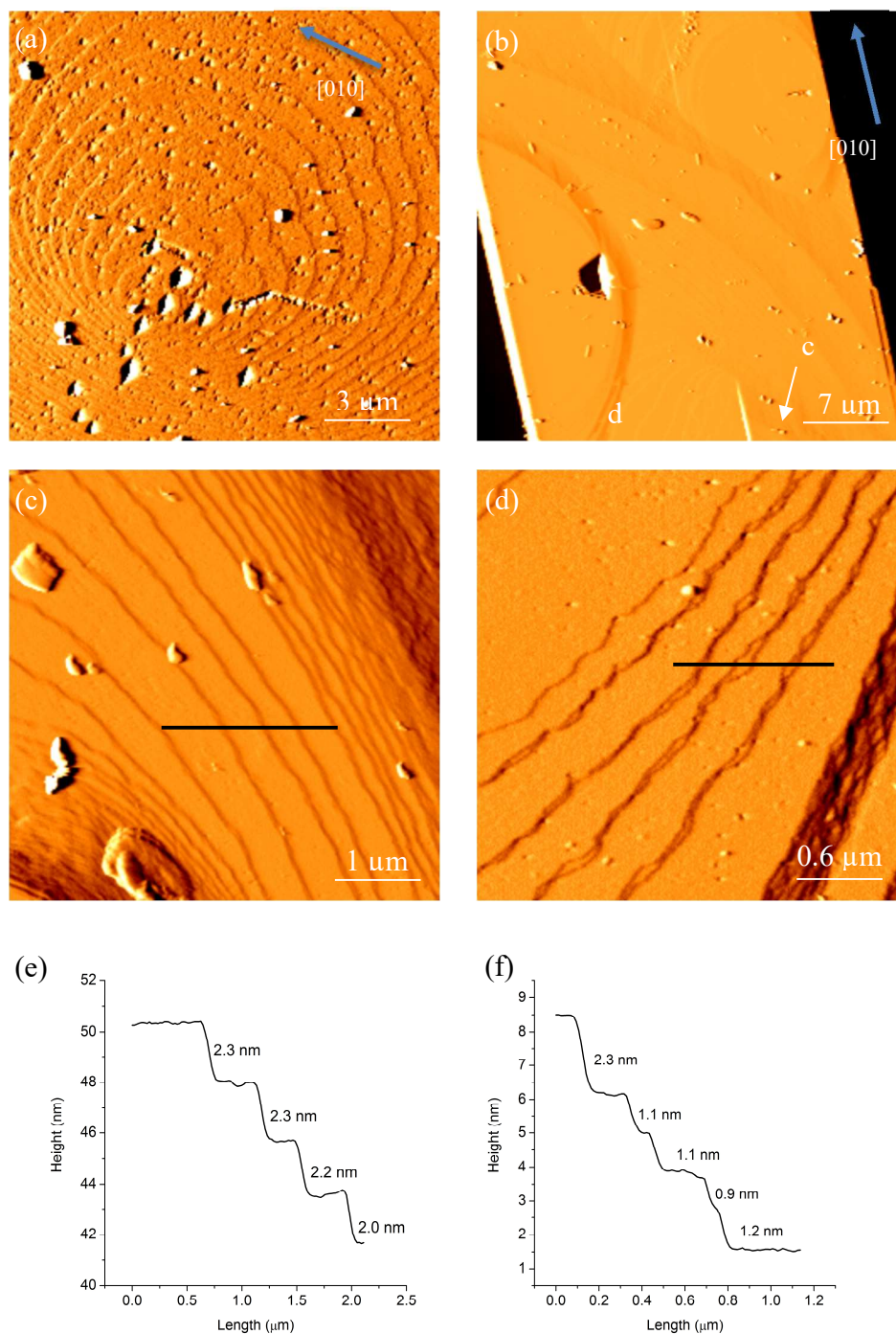


Figure 4-11 AFM deflection images captured on the surface of CaSDB from synthesis A. (a) was taken from the single crystal shown in Figure 4-10a; (b)-(d) were taken from the single crystal in Figure 4-10b. (e) and (f) are cross-sectional profiles along the line in (c) and (d), respectively.

On the CaSDB surfaces from synthesis A, growth hillocks are observed to adopt a round shape, which implies that the spreading of the layers is isotropic; whereas some other layers adopt an ellipse shape that is more extended towards [010]. Two typical examples are shown in Figure 4-11a and 4-11b, with Figure 4-11c and 4-11d being the zoom-in images from 4-11b. Growth behavior on planes observed is found to follow the “birth and spread” mechanism, evident due to the layered hillocks observed. A cross-sectional analysis was conducted on the layered structure in the hope of understanding its basic composition. Multiple heights are identified for the layers; they are 2.0 nm, 2.2 nm, and 2.4 ± 0.1 nm. Careful examination reveals that the steps are not the most basic growth units. In Figure 4-11d, it can be seen that the dominantly observed 2 nm layers are actually macro-steps that consist of two smaller layers. Three distinguishable heights were identified for the smallest layer, which are 0.9, 1.1 and 1.2 ± 0.1 nm. The phenomenon of stacked layers is referred to as “step bunching,” where the advance rate of the bottom layer is retarded so that the top layer could catch up to form a “bunch.” Theoretical studies have shown that the bunching behavior could be caused by multiple factors, including the anisotropic diffusion rates of building units to the surface and the presence of impurities.¹⁷⁻¹⁸

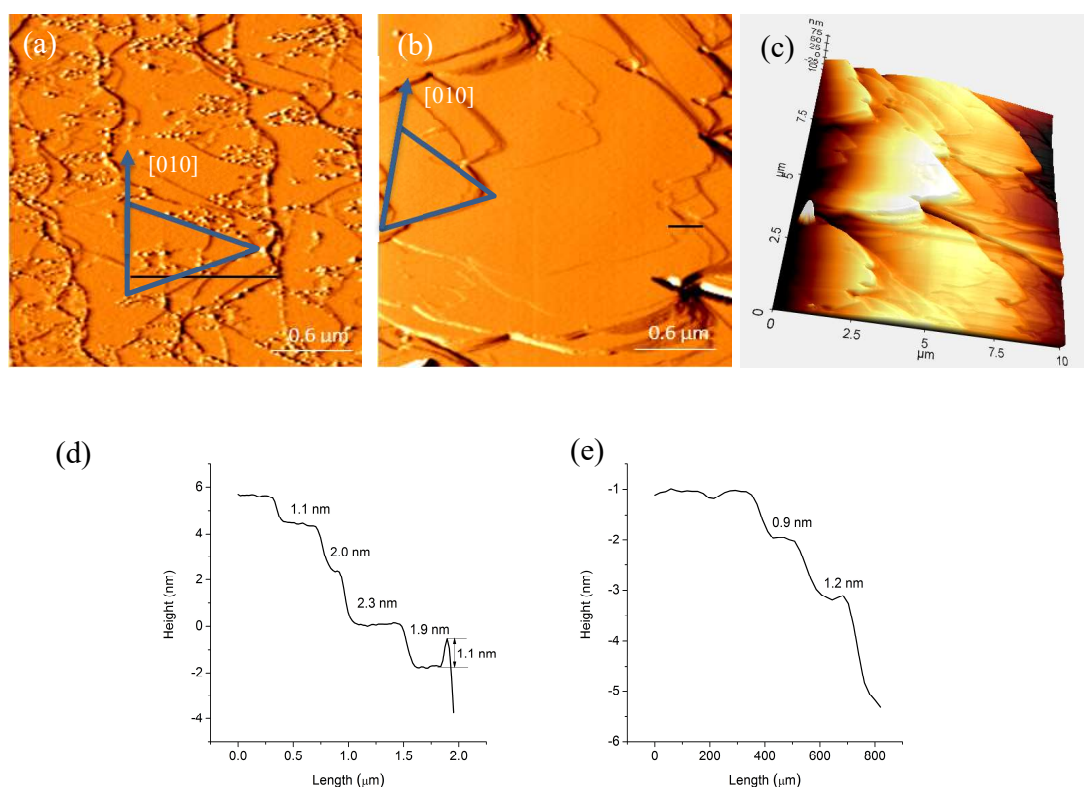


Figure 4-12 (a) and (b) are AFM deflection images and (c) is a topology image captured on the surface of CaSDB, showing triangular-like terraces. (d) and (e) are cross-sectional profiles along the black lines in (a) and (b), respectively.

In synthesis B where the starting amount of BDCA was doubled (Table 4-1), a second type of geometric layer pattern can be identified. Examples are shown in Figure 4-12. On those surfaces, the layer appears to adopt a pattern of isosceles triangles if we consider the base side parallel to [010]. However, only two sides of the triangle can be identified as growth steps, as outlined in Figure 4-12. Height profile captured along the steps shows that there is no noticeable difference between triangular layers and round layers in terms of step height: the same three basic heights, 0.9, 1.1 and 1.2 ± 0.1 nm, can be identified.

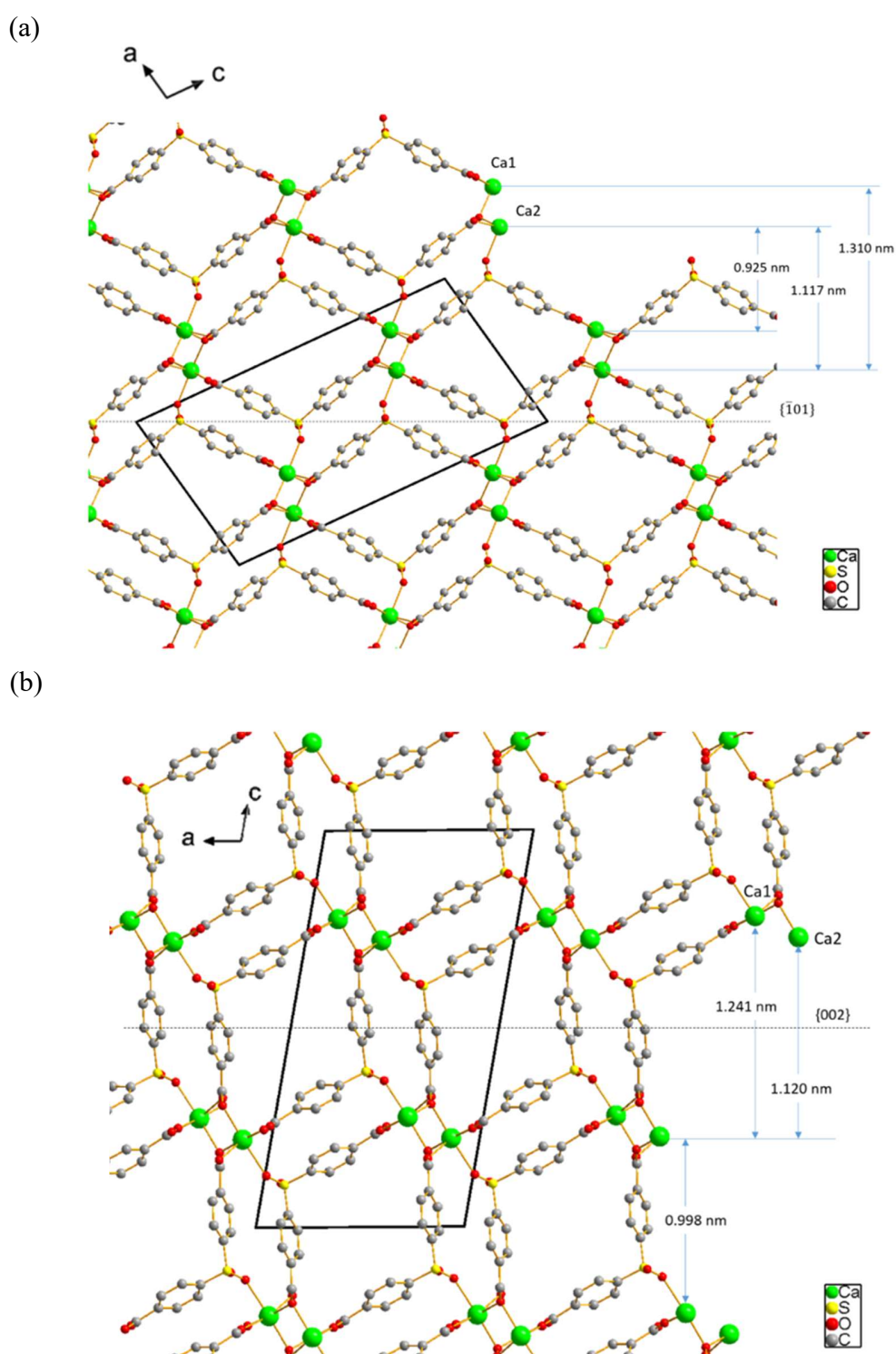


Figure 4-13 CaSDB framework structure viewing through [010] direction. The black box represents the unit cell.

Here attempts were made to correlate the observed layer heights to CaSDB's internal structure to further the understanding of its surface compositions. In the BFDH morphology calculation, $\{\bar{1}01\}$ and $\{002\}$ are the most prevalent faces.

As shown in Figure 4-13, on a given layer, the upper Ca ion is labeled as Ca1 whereas the lower Ca ion is labeled as Ca2. The 1.117 nm $d_{\bar{1}01}$ spacing (Figure 4-13a) and 1.120 nm d_{002} spacing (Figure 4-13b) can correspond to the distance between two closest Ca1 or Ca2 ions. The spacing between two adjacent Ca1, and Ca2 ions are also labeled. It can be seen that the differences between $\{\bar{1}01\}$ and $\{002\}$ spacings are less than 0.1 nm. Thus the observed steps heights can be claimed to correspond to the crystallographic spacings from either $\{\bar{1}01\}$ or $\{002\}$ within the 0.1 nm uncertainty.

Regarding face assignments, there exist two possibilities. One is that $\{\bar{1}01\}$ and $\{002\}$ planes are both present in the crystal habit, but they are indistinguishable solely from height analysis. Alternately, the surfaces showing different terrace patterns could be crystallographically equivalent. In that case, the round and triangular patterns were just reflections of growth anisotropies under the two different crystallization conditions. Even though no definite conclusion regarding Miller index assignation can be drawn from current experimentation, the results show the evidence that there exist two termination Ca ions on the surfaces of CaSDB.

4.3.3 CdSDB

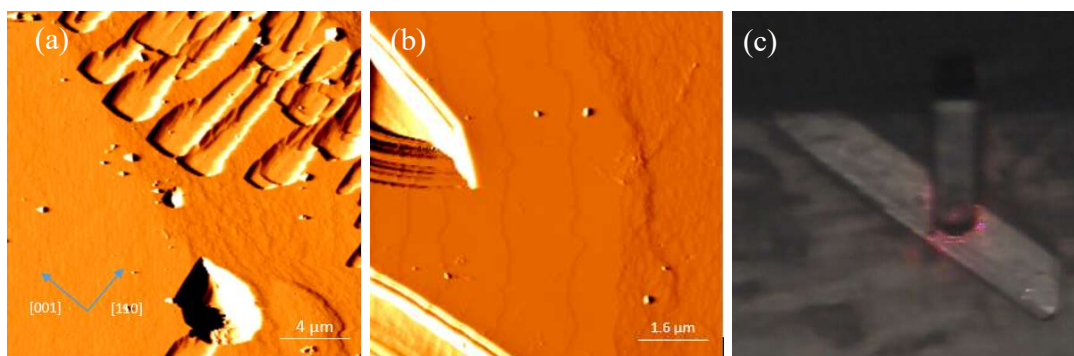


Figure 4-14 AFM deflection images of $\{110\}$ surface of CdSDB. (c) is the optical image of the single crystal being scanned.

In this section, another SDB MOF, CdSDB, is examined by AFM. They were synthesized hydrothermally. Single crystals adopt a morphology of four-fold prism that averagely has 1000 μm length and 100 μm in width. According to the BFDH calculation, the side faces observed are assigned to $\{110\}$ faces due to its largest relative area (43.6%). Figure 4-14 shows the AFM images captured on one of its faces. Again, a layered pattern can be observed, which indicates the growth mechanism to be “birth and spread.” Figure 4-14(a) highlights the presence of some rectangular blocks with edges parallel to $[110]$ and $[001]$ accordingly. However, since basic terraces observed do not adopt the rectangular shape, it is assumed that those hillocks were independent smaller crystals that adhere onto the surface. Some studies suggest that if given enough time, such smaller crystallites could be fully incorporated into the framework as growth proceeds.¹⁹⁻²⁰ For the basic terraces, no polygonal shape can be recognized.

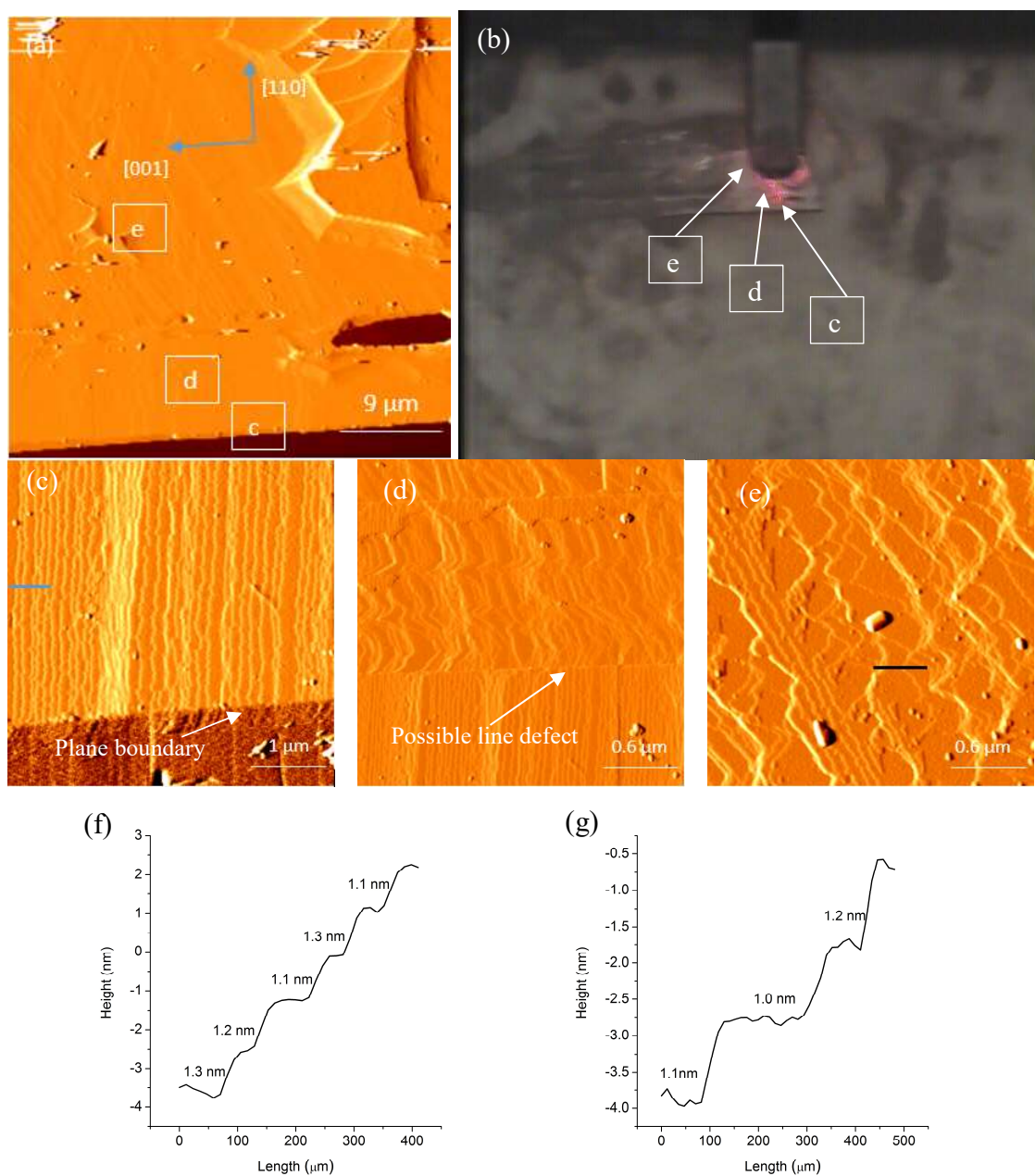


Figure 4-15 (a), (c-e) are the AFM deflection images captured on the surface of CdSDB and (b) is the single crystal's optical image. (c), (d), and (e) were captured from different regions on (a). (f) and (g) are cross-sectional profiles along the line in (c) and (e), respectively.

Observations were also made on several other single crystals of CdSDB. In an example shown in Figure 4-15, it can be seen that at different regions terraces follow different

directions. Near the crystal edge, the steps are roughly perpendicular to the $[001]$ direction (Figure 4-15c), whereas in the middle part the terraces are more disordered (Figure 4-15e). Figure 4-15d shows that there possibly exists a line defect that separates the two regions, and layers stop to spread when they hit the line.²¹ Height analysis was performed on the layers located in both areas, but no difference can be probed in terms of step height. Unfortunately, no explanation behind the observed various terrace morphologies can be provided without further experimentation.

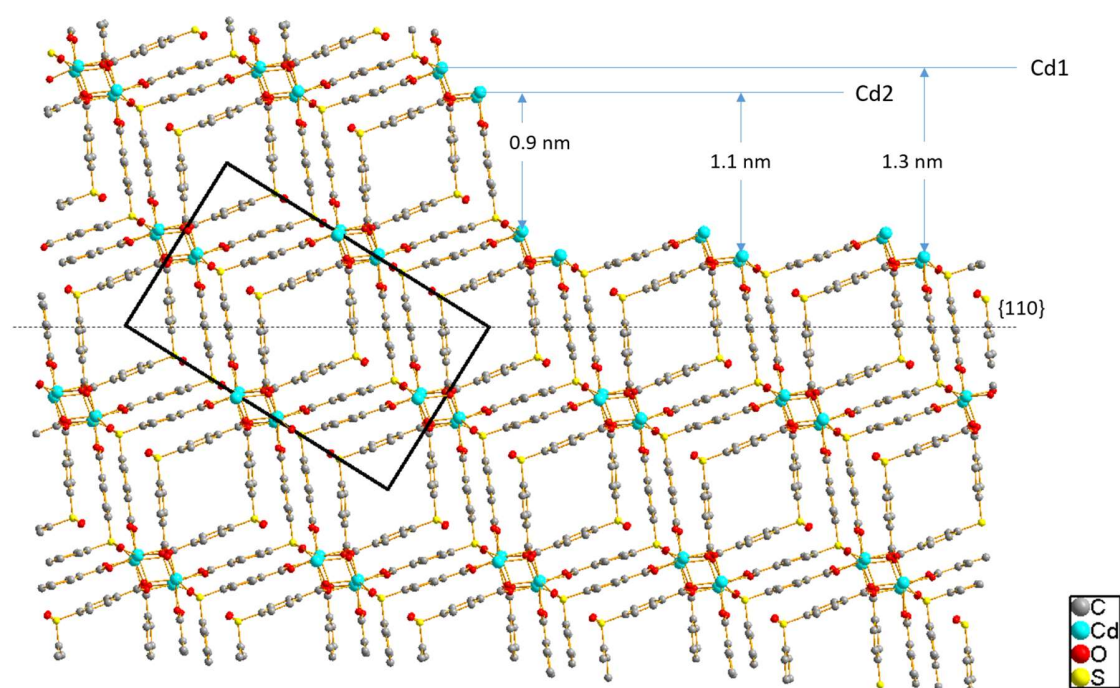


Figure 4-16 CdSDB framework structure viewing through $[001]$ direction. The black box represents the unit cell.

Similar to its Pb and Ca analogs, the two different positioned Cd ions are found to be responsible for the different heights observed. As shown in Figure 4-16, the d_{110} crystallographic spacing is 1.1 nm. However, the Cd ions are not perfectly aligned along $[001]$. As a result, the distances will slightly vary when measuring between adjacent Cd

ions, but they are observed to all drift around 0.9, 1.1 and 1.3 nm. Impressions are that 0.9 nm steps are much less seen. As shown in Figure 4-15, only one step with the height of 1.0 nm can be claimed to be in agreement with the 0.9 nm theoretical spacing. However, no quantitative measurements can be conducted to support that statement.

In summary, the surface terrace pattern on the surfaces of CdSDB is more chaotic than other MOFs we have studied, and at the current stage, we were unable to correlate the pattern with the framework's symmetry elements. However, like its Pb and Ca analogs, more than one monolayer heights can be identified for CdSDB.

4.4 Conclusion

AFM studies conducted provide information that helps understand the crystallization process of MOFs under different conditions. In our study, single crystals of PbSDB, CaSDB, CdSDB were successfully prepared and examined by AFM. It is found that all synthesized MOFs grow following the “birth and spread” mechanism and analyses of their morphology and height successfully relate the observations with their crystal structure. For PbSDB, we were able to observe two different sets of planes, $\{101\}$ and $\{002\}$, that have different surface morphologies. Surfaces of CaSDB single crystals presented a less ordered terrace shape, and attempts were made to figure out their Miller Indices assignation. For CdSDB, AFM measurement was carried out in multiple regions across the surface, and differences in terrace morphologies were discussed. For the three MOFs, basic layers that possess more than one unit heights can be observed, which could be explained by the presence of two differently positioned metal ions. Those findings suggest that the surface termination with two uniquely positioned metal centers seem to be common for SDB-based MOFs.

4.5 References

1. Lin, J.-D.; Wu, S.-T.; Li, Z.-H.; Du, S.-W., A Series of Novel Pb (II) or Pb (II)/M (II)(M= Ca and Sr) Hybrid Inorganic–Organic Frameworks Based on Polycarboxylic Acids with Diverse Pb–O–M (M= Pb, Ca and Sr) Inorganic Connectivities. *CrystEngComm* **2010**, *12* (12), 4252-4262.
2. Banerjee, D.; Zhang, Z.; Plonka, A. M.; Li, J.; Parise, J. B., A Calcium Coordination Framework Having Permanent Porosity and High CO₂/N₂ Selectivity. *Crystal Growth & Design* **2012**, *12* (5), 2162-2165.
3. Plonka, A. M.; Banerjee, D.; Woerner, W. R.; Zhang, Z.; Li, J.; Parise, J. B., Effect of Ligand Geometry on Selective Gas-Adsorption: The Case of a Microporous Cadmium Metal Organic Framework with a V-Shaped Linker. *Chemical Communications* **2013**, *49* (63), 7055-7057.
4. Chen, S.; Lucier, B. E.; Boyle, P. D.; Huang, Y., Understanding the Fascinating Origins of CO₂ Adsorption and Dynamics in MOFs. *Chemistry of Materials* **2016**, *28* (16), 5829-5846.
5. Plonka, A. M.; Banerjee, D.; Woerner, W. R.; Zhang, Z.; Nijem, N.; Chabal, Y. J.; Li, J.; Parise, J. B., Mechanism of Carbon Dioxide Adsorption in a Highly Selective Coordination Network Supported by Direct Structural Evidence. *Angewandte Chemie International Edition* **2013**, *52* (6), 1692-1695.
6. Hobbs, J. K.; Farrance, O. E.; Kailas, L., How Atomic Force Microscopy Has Contributed to Our Understanding of Polymer Crystallization. *Polymer* **2009**, *50* (18), 4281-4292.

7. Moh, P. Y.; Cubillas, P.; Anderson, M. W.; Attfield, M. P., Revelation of the Molecular Assembly of the Nanoporous Metal Organic Framework ZIF-8. *Journal of the American Chemical Society* **2011**, *133* (34), 13304-13307.
8. Wagia, R.; Strashnov, I.; Anderson, M. W.; Attfield, M. P., Determination of the Preassembled Nucleating Units that are Critical for the Crystal Growth of the Metal–Organic Framework CDIF-4. *Angewandte Chemie International Edition* **2016**, *55* (31), 9075-9079.
9. Smith, R. L.; Lind, A.; Akporiaye, D.; Attfield, M. P.; Anderson, M. W., Anatomy of Screw Dislocations in Nanoporous SAPO-18 as Revealed by Atomic Force Microscopy. *Chemical Communications* **2015**, *51* (28), 6218-6221.
10. Cubillas, P.; Anderson, M. W.; Attfield, M. P., Influence of Isomorphous Substituting Cobalt Ions on the Crystal Growth of the MOF-5 Framework Determined by Atomic Force Microscopy of Growing Core-Shell Crystals. *Crystal Growth & Design* **2013**, *13* (10), 4526-4532.
11. McPherson, A.; Malkin, A.; Kuznetsov, Y. G., Atomic Force Microscopy in the Study of Macromolecular Crystal Growth. *Annual Review of Biophysics and Biomolecular Structure* **2000**, *29* (1), 361-410.
12. Banerjee, D.; Simon, C. M.; Plonka, A. M.; Motkuri, R. K.; Liu, J.; Chen, X.; Smit, B.; Parise, J. B.; Haranczyk, M.; Thallapally, P. K., Metal-Organic Framework with Optimally Selective Xenon Adsorption and Separation. *Nature Communications* **2016**, *7*, 11831.

13. Xiao, D.; Chen, H.; Sun, D.; Zhang, G.; He, J.; Yuan, R.; Wang, E., A 3d Interpenetrated Rutile Coordination Framework Formed by Dinuclear Cadmium Clusters and 4, 4'-Sulfonyldibenzoate. *Solid State Sciences* **2011**, *13* (8), 1573-1578.
14. Bishop, A. C., *An Outline of Crystal Morphology*. Hutchinson Scientific and Technical: London, 1967.
15. Sunagawa, I., *Crystals : Growth, Morphology, and Perfection*. Cambridge University Press: Cambridge, 2005.
16. De Yoreo, J. J.; Vekilov, P. G., Principles of Crystal Nucleation and Growth. *Reviews in Mineralogy and Geochemistry* **2003**, *54* (1), 57-93.
17. Kandel, D.; Weeks, J. D., Step Bunching as a Chaotic Pattern Formation Process. *Physical Review Letters* **1992**, *69* (26), 3758.
18. Kandel, D.; Weeks, J. D., Theory of Impurity-Induced Step Bunching. *Physical Review B* **1994**, *49* (8), 5554.
19. McPherson, A.; Kuznetsov, Y. G., Mechanisms, Kinetics, Impurities and Defects: Consequences in Macromolecular Crystallization. *Acta Crystallographica Section F: Structural Biology Communications* **2014**, *70* (4), 384-403.
20. Malkin, A. J.; Kuznetsov, Y. G.; McPherson, A., Incorporation of Microcrystals by Growing Protein and Virus Crystals. *Proteins: Structure, Function, and Bioinformatics* **1996**, *24* (2), 247-252.
21. Mullin, J. W., *Crystallization*. Butterworth-Heinemann: Oxford, 2001.

Chapter 5

5 Summary and Future Works

5.1 Summary

The overall goal of the thesis is to better understand the crystal growth process of Metal-Organic Frameworks. The results have proven that Atomic Force Microscopy is a very powerful tool in observing and elucidating surface growth features of MOFs.

Experimental results were discussed in two of the chapters. In Chapter 2, a flexible Metal-Organic Framework, Ga-MIL-53, was studied. We examined the surface growth patterns on $\{101\}$ faces, and also determined the surface unit structure by performing height analyses. The surface growth was found to mostly follow the “birth and spread” mechanism with rectangular growth hillocks, while a specific growth spiral was also successfully captured by AFM, indicating the presence of “spiral growth” mechanism. Observations of the surfaces developed with different synthesis times reveal that terraces do not always adopt a rectangular shape. For crystals with a 12 hour to 1 day synthesis time, the terraces adopt a hexagonal shape, whereas for crystals obtained after more than 3 days of synthesis time, a majority of the terraces observed are rectangular. In comparison, a transitional form of octagon-shaped terraces can be observed on surfaces with a synthesis time between 1 to 3 days. These findings suggest that the relative growth rates along different crystallographic directions may change before product crystallization is complete. Various synthesis attempts were also made in an effort to investigate the effect of starting metal to ligand ratio. It was found that when the starting Ga/BDCA ratio was increased from 1:2 to 1:1, no rectangular terrace could be developed and the terrace morphology shares similarities with the hexagonal terraces observed in 1-day samples. Observations were also

made on surfaces of Ga-MIL-53 after phase transition known as “breathing effect.” Frequent fracturing was observed after the channel occupants were changed.

Chapter 3 studies the Pb, Ca and Cd analogs of M-SDB MOFs, which form a framework with SDB as the organic ligand. “Birth and spread” growth mechanism were found to be followed for surface growth occurring on all three MOFs. Interestingly, more than one basic step heights could be identified. By relating those heights to plausible crystal structure spacings, it was inferred that the growth steps with different heights were due to surface termination between two differently positioned metal centers.

5.2 Future Works

In Chapter 2, we proposed that terrace will develop into different shapes as it grows with time. However, no direct evidence can be provided from current experimentation. Currently, *in-situ* AFM experiments are not available for MOFs prepared by hydrothermal methods. Thus it would be interesting to explore the possibilities of non-hydrothermal methods for those materials to perform real-time monitoring of the surface growth.

In Chapter 3, we were unable to assign the definite Mill Index for CaSDB single crystals from merely BFDH calculations and AFM measurements. Thus in the future, it would be ideal if a more accurate method could be used to determine the Mill Indices of crystal planes, i.e. surface free energy/attachment energy calculations or single crystal X-ray diffraction experiments. Additionally, more experiments could be conducted to explore how the complicated surface features of CdSDB can be related to its internal symmetry and growth conditions.

MOFs with a flexible network have received great interest due to their tunable pore size. In our study, only the Gallium analog of the MIL-53 MOF was studied, partially because it could be easily obtained in the form of large single crystals. It has been reported that single crystals of Al-MIL-53 could also be grown when HF is added during the crystallization process.¹ Thus performing AFM observations on the Al analog may yield interesting results complimentary to our work conducted on Ga-MIL-53.

For the MOFs studied in this work, the formation of frameworks only involves one type of ligand. Recently, a type of framework which features a “layered-pillared” structure has been reported in literature.²⁻³ For example, the MOF $\text{Zn}_2(\text{Atz})_2\text{O}_x$ is composed of 2D Zinc-aminotriazolate layers pillared by oxalate acid to form a 3D network. The presence of two distinct ligands could potentially give rise to surface structures with different heights. Thus AFM could be used to study the surface growth of this type of MOFs due to its high resolution in the z direction. Additionally, it would be interesting to perform *in-situ* AFM experiments on those MOFs in order to answer questions such as how the 2D layers are cross-linked by a different ligand during the self-assembly process.

5.3 References

1. Vougo-Zanda, M.; Huang, J.; Anokhina, E.; Wang, X.; Jacobson, A. J., Tossing and Turning: Guests in the Flexible Frameworks of Metal (III) Dicarboxylates. *Inorganic Chemistry* **2008**, 47 (24), 11535-11542.
2. Banerjee, A.; Nandi, S.; Nasa, P.; Vaidhyanathan, R., Enhancing the Carbon Capture Capacities of a Rigid Ultra-Microporous MOF through Gate-Opening at Low CO_2 Pressures Assisted by Swiveling Oxalate Pillars. *Chemical Communications* **2016**, 52 (9), 1851-1854.

3. Dybtsev, D. N.; Chun, H.; Kim, K., Rigid and Flexible: A Highly Porous Metal-Organic Framework with Unusual Guest-Dependent Dynamic Behavior. *Angewandte Chemie* **2004**, *116* (38), 5143-5146.

Appendices

Permissions Sales UK <Rights@cambridge.org>

Thu 2017-09-07 9:45

To Zitong Wang

Dear Customer

Thank you for your request to reproduce one figure in your forthcoming PhD thesis, for non-commercial publication. Cambridge University Press are pleased to grant non-exclusive permission, free of charge, for this specific one time use, on the understanding you have checked that we do not acknowledge any other source for the material. This permission does not include the use of copyright material owned by any party other than the author/s. Consent to use any such material must be sought by you from the copyright owner concerned.

Please ensure full acknowledgement appears in your work.

Should you wish to publish your work commercially in the future, please reapply to the appropriate Cambridge University Press office, depending on where your forthcoming work will be published. Further information can be found on our website at the following link:

<http://www.cambridge.org/about-us/rights-permissions/permissions/>

Permissions Sales team

Cambridge University Press

<http://www.cambridge.org/about-us/rights-permissions/permissions/>

Appendix 1 Copyright permission for Figure 1-1 and 1-2.

**Mineralogical Society of Great Britain and Ireland LICENSE
TERMS AND CONDITIONS**

Sep 06, 2017

This is a License Agreement between University of Western Ontario -- Zitong Wang ("You") and Mineralogical Society of Great Britain and Ireland ("Mineralogical Society of Great Britain and Ireland") provided by Copyright Clearance Center ("CCC"). The license consists of your order details, the terms and conditions provided by Mineralogical Society of Great Britain and Ireland, and the payment terms and conditions.

All payments must be made in full to CCC. For payment instructions, please see information listed at the bottom of this form.

License Number	4183330666822
License date	Sep 06, 2017
Licensed content publisher	Mineralogical Society of Great Britain and Ireland
Licensed content title	The Mineralogical magazine and journal of the Mineralogical Society
Licensed content date	Jan 1, 1876
Type of Use	Thesis/Dissertation
Requestor type	Academic institution
Format	Electronic
Portion	image/photo
Number of images/photos requested	1
Title or numeric reference of the portion(s)	Fig 1-3
Title of the article or chapter the portion is from	Changes in Habit During the Growth of Baryte Crystals from the North of England
Editor of portion(s)	N/A
Author of portion(s)	Seager, A.; Davidson, W.
Volume of serial or monograph.	29
Issue, if republishing an article from a serial	217
Page range of the portion	886
Publication date of portion	November 2, 1950
Rights for	Main product
Duration of use	Life of current edition
Creation of copies for the disabled	no
With minor editing privileges	no
For distribution to	Canada
In the following language(s)	Original language of publication
With incidental promotional use	no
The lifetime unit quantity of new product	Up to 499
Made available in the following markets	education

Appendix 2 Copyright permission for Figure 1-3

**ROYAL SOCIETY OF CHEMISTRY LICENSE
TERMS AND CONDITIONS**

Sep 06, 2017

This Agreement between University of Western Ontario -- Zitong Wang ("You") and Royal Society of Chemistry ("Royal Society of Chemistry") consists of your license details and the terms and conditions provided by Royal Society of Chemistry and Copyright Clearance Center.

License Number	4183331433396
License date	Sep 06, 2017
Licensed Content Publisher	Royal Society of Chemistry
Licensed Content Publication	CrystEngComm
Licensed Content Title	Crystal form, defects and growth of the metal organic framework HKUST-1 revealed by atomic force microscopy
Licensed Content Author	Maryiam Shōâëè,Jonathan R. Agger,Michael W. Anderson,Martin P. Attfield
Licensed Content Date	Feb 18, 2008
Licensed Content Volume	10
Licensed Content Issue	6
Type of Use	Thesis/Dissertation
Requestor type	academic/educational
Portion	figures/tables/images
Number of figures/tables/images	2
Format	electronic
Distribution quantity	500
Will you be translating?	no
Order reference number	
Title of the thesis/dissertation	Investigating Growth of Metal-Organic Frameworks via Atomic Force Microscopy
Expected completion date	Sep 2017
Estimated size	100

Appendix 3 Copyright permission for Figure 1-6.



Copyright
Clearance
Center



Home

Account Info

Help





ACS Publications
Most Trusted. Most Cited. Most Read.

Title: Revelation of the Molecular Assembly of the Nanoporous Metal Organic Framework ZIF-8

Author: Pak Y. Moh, Pablo Cubillas, Michael W. Anderson, et al

Publication: Journal of the American Chemical Society

Publisher: American Chemical Society

Date: Aug 1, 2011

Copyright © 2011, American Chemical Society

Logged in as:
Zitong Wang
University of Western Ontario

Account #:
3001192321

LOGOUT

PERMISSION/LICENSE IS GRANTED FOR YOUR ORDER AT NO CHARGE

This type of permission/license, instead of the standard Terms & Conditions, is sent to you because no fee is being charged for your order. Please note the following:

- Permission is granted for your request in both print and electronic formats, and translations.
- If figures and/or tables were requested, they may be adapted or used in part.
- Please print this page for your records and send a copy of it to your publisher/graduate school.
- Appropriate credit for the requested material should be given as follows: "Reprinted (adapted) with permission from (COMPLETE REFERENCE CITATION). Copyright (YEAR) American Chemical Society." Insert appropriate information in place of the capitalized words.
- One-time permission is granted only for the use specified in your request. No additional uses are granted (such as derivative works or other editions). For any other uses, please submit a new request.

Appendix 4 Copyright permission for Figure 1-7.

Curriculum Vitae

Name: Zitong Wang

Post-secondary Education and Degrees: The University of Western Ontario
London, Ontario, Canada
2011-2015 B.Sc.

The University of Western Ontario
London, Ontario, Canada
2015-2017 M.Sc.

Related Work Experience: Teaching Assistant
The University of Western Ontario
2015-2017

Presentations:

1. Wang, Z., Nie, H.-Y., Huang, Y., (2016), *Investigating Growth of the Ga-MIL-53 and PbSDB Microporous Metal-Organic Frameworks via Atomic Force Microscopy*, Oral presentation, 49th Inorganic Discussion Weekend, Hamilton, Ontario.
2. Wang, Z., Nie, H.-Y., Huang, Y., (2017), *An Investigation of Crystal Growth of Metal-organic Frameworks by AFM*, Poster presentation, 19th International Scanning Probe Microscopy Conference, Sakyo-ku, Kyoto, Japan.
3. Wang, Z., Nie, H.-Y., Zhang, Y., Huang, Y., (2017), *Investigating Growth of the Ga-MIL-53 Metal-organic Frameworks via Atomic Force Microscopy*, Poster presentation, 100th Canadian Chemistry Conference and Exhibition, Toronto, Ontario.